NTNU – Trondheim
Norwegian University of
Science and Technology

Pressure Fluctuations and Correlations in Steady State two Phase Flow in Porous Media

Sjur Peder Helland

Master of Science in Physics and Mathematics
Submission date: June 2013
Supervisor: Alex Hansen, IFY

Norwegian University of Science and Technology
Department of Physics

Pressure fluctuations and correlations in two dimensional steady state flow in porous media

Sjur Peder Helland

June 23, 2013

Abstract

This thesis investigates the burst size distribution and pressure correlation profiles of steady state two phase flow in porous media at various capillary numbers and viscosity ratios. A network model is used to simulate steady state flow in a two dimensional porous media by simultaneous injection of both the wetting and the non-wetting phase. The steady state burst size distribution is found to be a power law with critical exponent $\alpha = -2.0134 \pm 0.13$. The distribution is found to be independent of capillary number and viscosity ratio. This is consistent with earlier results found for the burst size distribution during invasion and with other systems exhibiting self organized criticality. The two point pressure correlation is estimate by curve fitting. The fitted curve is found to scale as a power law with critical exponent $\eta = 1/2$ in the long range limit.

Preface

The project was completed in collaboration with Daniel Lisø. I want to thank Daniel for the many hours we spent together working on this project and for the significant amount of coffee I owe him by now.

I would like to extend my appreciation to our supervisor Alex Hansen for assigning us this interesting topic and for his helpful comments and guidance along the way. I also wish to thank Alex for introducing me to the field of computational physics through the course he teaches at NTNU.

I am particularly grateful for the assistance given by Santanu Sinha who wrote the majority of the simulation program we used and without who's help this project would have been impossible. We appreciate the time he took to explain various aspects of the program and the help he provided us in modifying it.

Furthermore I wish to acknowledge the assistance provided by Ken Tore Tallakstad who was very helpful with providing information about the experiments performed at the University of Oslo.

In addition I would like to acknowledge everyone in the flow in porous media group at NTNU, who's input during our weekly meetings helped us explore new ideas and learn about other areas within the fascinating field of flow in porous media.

Finally I want to thank Johannes Ofstad for the time he spent proof-reading this thesis and Ken Vidar Falch for his helpful comments and ideas.

Sjur Peder Helland, June 2013

Contents

1 Introduction

Flow in porous media is a subject of significant interest because of it's practical applications in a wide range of fields from medicine to hydrology and oil recovery. Early studies conducted often concerned themselves with the practical applications with little regard for the exact nature of the flow. An example of such early measurements was the measurement of permeabilities of core samples in laboratories [32, 36].

Multiphase flow in porous media is also an interesting system in physics because of the complex structures formed during the process. The large three dimensional core samples used in earlier experiments are unsuited for studying these structures so more suited experiments had to be designed. Early experiments studied the dynamics of two-phase flow through networks etched in glass [23] or in Hele-Shaw cells [30, 33]. Much of this early work studied the displacement process, where one fluid inhabits a porous medium and a second fluid is injected into the medium, displacing the first fluid. This system creates a rich variety of displacement structures based on the a limited number of parameters. As a result of this work various flow regimes were identified and successfully modelled with simple geometric algorithms [12, 13, 24, 25, 30, 34, 43, 44].

Later experiments were designed to study steady state flow in porous medium. In these experiments both fluids are injected into the medium simultaneously. This results in complex flow patterns. The earliest steady state experiment studying the flow on the pore scale was conducted by Payatakes et. al. [6, 7] who aimed to study pore scale dynamics influence on measure relative permeabilities. Since then multiple aspects of steady state flow has been studied both experimentally and numerically. Despite this, multi phase flow is still not as well understood as the invasion process.

Aker. et. al. studied pressure fluctuations during and invasion process. Through this the distribution of so called bursts was determined to be a power law with critical exponent $\alpha = 1.9 \pm 0.1$, independent of all relevant flow parameters [5]. This was done both experimentally and numerically using a network model to simulate the flow. In this thesis we numerically determine the burst size distribution of steady state flow and how this distribution depends on the capillary number and the viscosity ratio. This is done using a slightly altered version of the model used by Aker et. al. In addition to the burst size distribution the spatial and temporal

pressure variation in the porous media is studied. From this the correlation function's temporal and spatial scaling is determined.

This thesis is organized into five sections. Section 2, immediately following the introduction, contains a short review of the basic physical principles and equations governing two phase flow in porous media. This is followed by a qualitative description of various flow regimes during two phase flow. Finally correlation functions and power laws are briefly discussed. Section 3 describes the network model and the various techniques used in the data analysis as well as the actual parameters used during the simulations. Section 4 contains the results along with a discussion of the results, while section 5 contains our concluding remarks. The appendices contain various mathematical details along with a small network example of the model that was used.

2 Theory

2.1 Porous media

A porous medium is a solid material containing interconnected voids of various sizes. These voids are called the pores. A characteristic property of the porous medium is the porosity or void fraction, defined as

$$\phi = \frac{V_{\text{void}}}{V_{\text{total}}} \tag{2.1}$$

where V_{void} is the total volume of the pores and V_{total} is the total volume of media. Porous media are frequently found in nature with typical examples being sandstone and limestone. Several exotic engineered materials are also porous media. For instance the super light aerogel derives many of its physical properties from a very high void fraction, sometimes as high as $\phi \approx 0.99$ [35].

The permeability of the media, K, is also of significant interest. Permeability is a measure of a materials ability to allow a fluid to pass through it, and is consequently of interest during oil recovery. It is a geometric property that depends only on the pore size and configuration in the material. Permeability can be viewed as the fluid mechanical equivalent of conductance from electronics. Permeability describes the flow through the medium when exposed to a pressure difference just as conductance measures the current through a conductor exposed to a voltage difference. Permeability is a factor in the proportionality constant of Darcy's law, see section 2.3, and is defined as:

$$K = v\frac{\mu \Delta x}{\Delta P} \tag{2.2}$$

where v is bulk flow rate through the medium, μ is the viscosity, Δx is the length of the medium and ΔP is the pressure difference.

Because porosity and permeability are of particular interest during oil recovery multiple techniques have emerged to measure them. One particular such measurement, using a nuclear magnetic resonance technique at a gulf coast oil field found porosity in the range $\phi \approx 5 - 30$ and permeability in the range $k \approx 10 - 10^3\,\text{mD}$ [41]. Where mD is one milli darcy and one darcy is equivalent to $9.87 \cdot 10^{-9}\,\text{cm}^2$. The measured material was mainly sandstone.

2.2 Flow in porous media

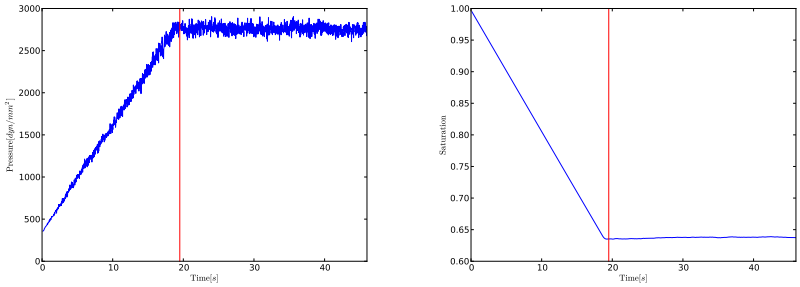

Figure 2.1: Pressure and wetting fluid saturation evolution. The red line indicates the end of the invasion phase and start of the steady state.

Typical evolution of pressure across the system and wetting phase saturation is displayed in figure 2.1. The wetting phase saturation, S, is defined as $S = V_{\text{wetting}}/V_{\text{total}}$. The plots are results from a network simulation. The network is initially occupied by the wetting fluid, with both the wetting and the non-wetting phase simultaneously injected at the boundary of the network. The pressure increases until the fluids reach a stable equilibrium, the steady state. The period while the pressure is increasing is called the transient phase or the invasion phase. This phase is briefly discussed in section 2.3.2, while discussion of the steady state begins from section 2.3.3.

2.2.1 Flow and fluid parameters

Capillary number

When considering slow multiphase flow through a horizontal network the dominating forces are the viscous forces and the capillary forces. The capillary number describes the ratio between these forces. The capillary number is defined as

$$Ca = \frac{\mu_{\text{eff}} Q_{\text{tot}}}{\gamma A} \tag{2.3}$$

where Q_{tot} denotes the total flow rate through the system, A is the cross section area and γ is the interface tension between the fluids. For large values, $Ca \approx 1$, the viscous forces dominate, while for low values, $Ca \ll 1$, the capillary forces dominate. Both quantitative and qualitative properties of the flow depend this ratio. The effect is most dramatic during the invasion phase as illustrated in section 2.3.2, however also steady state variables like the cluster size distribution depend on the capillary number [40].

Viscosity ratio

Viscosity is a measure of fluids resistance to deformation caused by stress. For Newtonian fluids it is a parameter that depends only on the temperature of the fluid. In two phase flow the viscosity ratio between the two fluid has large implications for the overall flow behaviour. It is customary to define the viscosity ratio M as

$$M = \frac{\mu_{\text{nw}}}{\mu_{\text{w}}} \tag{2.4}$$

where μ_{nw} and μ_{w} is the viscosity of the non-wetting and the wetting fluid respectively. In experimental studies it is often difficult to control this variable as the viscosity is highly dependent on temperature in complicated manners [14].

Wettability

The wettability is a fluid-surface property. When a fluid droplet is placed on a smooth solid surface adhesive forces between the fluid and the surface will force the droplet to spread out across the surface, increasing the contact surface. Cohesive forces within the droplet will simultaneously try to minimize the contact surface between the fluid and solid. The resulting shape is something resembling a truncated sphere, however the exact shape differs based on properties of both the fluid and the solid surface. The truncated sphere will meet the surface at some angle θ. This angle is called the contact angle and is inversely related to the wettability of the fluid-surface pair. Figure 2.2 shows a non-wetting and a wetting droplet on a plane surface with the contact angle indicated.

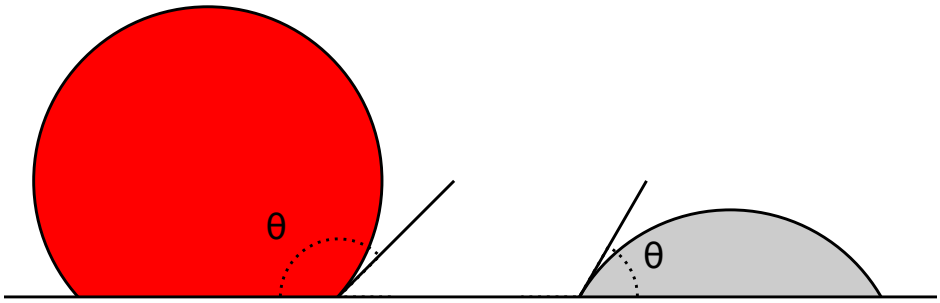

Figure 2.2: Wetting angle θ for a wetting (grey) and a non-wetting (red) fluid droplet on a smooth surface. Both fluids form truncated spheres, but with different contact angles and contact surfaces.

The contact angle is used to categorize fluids into wetting fluids and non-wetting fluids.

$$\text{Wetting} : 0^\circ \leq \theta \leq 90^\circ$$
$$\text{Non-wetting} : 90^\circ \leq \theta \leq 180^\circ$$

with the special cases $\theta = 0$ and $\theta = 180$ called perfect wetting and perfect non-wetting respectively. The wettability is of particular interest during invasion experiments as displacement of wetting fluid by a non-wetting fluid, called drainage, and the reverse process, called imbibition, is significantly different on the pore level. During steady state flow the distinction between imbibition and drainage disappears as both processes occur simultaneously.

The discussion has so far revolved around a static droplet on a static surface. This is called the static wettability. During flow in porous media the fluids are not static and the dynamic contact angle, θ_D, needs to be introduced. It has been observed that the contact angle of a fluid moving across a surface differs from the contact angle of the same fluid at rest on the same surface. Furthermore the contact angle of an advancing fluid differs from that of the same receding fluid. The exact nature of the difference in contact angle is an open problem with several plausible explanations [1]. Exactly measuring the angle is also difficult, but in general the

contact angle of an advancing fluid will increase with displacement rate, while the contact angle of a receding fluid will decrease with displacement rate [11].

Other fluid, flow and system properties

The interface tension γ is an important fluid-fluid property. During two phase flow in porous media the interface tension dictates the pressure difference required to move an interface, and consequently the flow rate is inversely dependent on γ as seen in equation 2.3. The shape and size of the pores will also influence the flow, via the capillary pressure.

2.3 Governing equations

Differential governing equations

On the pore level two-phase flow in porous media is a two-phase interface flow of newtonian fluids. As such it is theoretically possible to solve the Navier-Stokes and continuity equation for each pore and integrate over the entire system to get an exact solution of the flow through the medium. For a horizontal incompressible flow with no body forces acting upon the fluids Navier-Stoke equation reads:

$$\rho \frac{\partial \mathbf{u}}{\partial t} + \rho \mathbf{u} \cdot \nabla \mathbf{u} = -\nabla p + \mu \nabla^2 \mathbf{u} \tag{2.6}$$

And the continuity equation is given by:

$$\nabla \cdot \mathbf{u} = 0 \tag{2.7}$$

In both equation 2.6 and equation 2.7 $\mathbf{u}(\mathbf{x}, t)$ is the velocity, ρ is the fluid density and μ is the fluid viscosity. For multiphase flow the set of equations formed by equation 2.6 and 2.7 must be solved with the following boundary conditions

- The velocity of each fluid must be zero at the pore walls.
- The velocity must be equal in each of the fluids at the interface.
- The pressure difference imposed by the interface must be negated by the forces in each fluid.

The complex equation set along with these boundary conditions make it unfeasable to solve the problem directly using the exact governing equations.

Darcy's law

Darcy's law is an experimental result, obtained by studying the flow of water through a sand filled cylinder, however it has been found to apply a wide range of porous systems and fluids. The differential form of the law with no body forces acting on the system reads:

$$Q = -\frac{AK}{\mu}\nabla p \tag{2.8}$$

where A is the cross section area of the porous media normal to the flow direction, K is the permeability, μ is the viscosity and ∇p is the global pressure gradient. This relation applies to a single fluid flowing through a porous media. Even thought Darcy's law was originally a phenomenologically law it has since been derived from the Navier-Stokes equation through asymptotic homogenization [20]. Nonetheless it can not be expected to apply to an arbitrary flow, but it is assumed to be accurate as long as the flow rate is not very high [37].

Darcy's law can be generalized to apply to multiphase flow by introducing effective fluid parameters in the following way.

$$Q_{\mathrm{w}} = -\frac{AK_{\mathrm{w}}^{\mathrm{eff}}}{\mu_{\mathrm{w}}}\nabla p \tag{2.9a}$$

$$Q_{\mathrm{nw}} = -\frac{AK_{\mathrm{nw}}^{\mathrm{eff}}}{\mu_{\mathrm{nw}}}\nabla p \tag{2.9b}$$

where K^{eff} is the effective permeability. While the absolute permeability K is a material property that only depends on the geometry of the porous media, the effective permeability also depends on several flow parameters, including the capillary number, the viscosity ratio and the wettability.

Hagen–Poiseuille flow and the Washburn equation

The Hagen-Poiseuille equation describes the pressure drop in laminar flow through a circular tube with a constant cross section area. The equa-

tion has been successfully applied to a wide range of problems from flow through human capillaries to flow through drinking straws. The equation can be derived from the Navier-Stokes law by assuming that the flow is steady, fully developed and axis-symmetrical. It is also required that the radial and swirl components of the flow is zero. Under these conditions Navier-Stokes law, equation 2.6, is reduced to

$$\frac{1}{r}\frac{\partial}{\partial r}\left(r\frac{\partial u_x}{\partial r}\right) = \frac{1}{\mu}\frac{\partial p}{\partial x} \tag{2.10}$$

Solving this equation, with the no slip boundary condition, results in a parabolic velocity profile on the form:

$$u_x = -\frac{1}{4\mu}\frac{\partial p}{\partial x}\left(R^2 - r^2\right) \tag{2.11}$$

Averaging over the cross section gives the average velocity:

$$\langle u_x \rangle = \frac{1}{2}\frac{R^2}{4\mu}\left(-\frac{\partial p}{\partial x}\right) \tag{2.12}$$

Assuming that the pressure drops linearly along the length of the tube and rearranging the terms results in the Hagen–Poiseuille equation:

$$\Delta P = \frac{8\mu L Q}{\pi r^4} \tag{2.13}$$

where $\langle v_x \rangle$ has been multiplied with the cross section area to give the total flow rate, Q, and L is the length of the tube.

By expressing volume in terms of length and substituting for Q in the Hagen–Poiseuille equation Washburn obtained [42]:

$$\frac{\partial l}{\partial t} = \frac{\sum P}{8r^2\mu l}\left(r^4 + 4\epsilon r^3\right) \tag{2.14}$$

where the sum is over all participating pressures and ϵ is the coefficient of slip. For a horizontal flow network with the assumption that the wetting fluid perfectly wets the walls, equation 2.14 can be simplified to:

$$Q = -\frac{\pi r^2 k}{\mu}\frac{\sum P}{l} \tag{2.15}$$

where the permeability $k = r^2/8$ has been introduced. The permeability k is the permeability of the single circular tube and not equivalent to the medium permeability of Darcy's law. Note that the pressure sum, $\sum P$, runs over all pressure contributions including interface pressures.

Young-Laplace equation

The Young-Laplace equation describes the capillary pressure difference across the interface between two static fluids. The equation reads

$$\Delta p = -\gamma \left(\frac{1}{R_1} + \frac{1}{R_2} \right) \tag{2.16}$$

where Δp is the pressure difference, γ is the surface tension and R_1 and R_2 are the principal radii of curvature.

2.3.1 Drainage and imbibition

During a displacement process in a porous medium it is customary to refer to the fluid that is being displaced as the defending fluid and the fluid displacing it as the invading fluid. The process where a non-wetting fluid displaces a wetting fluid is called drainage, the reverse process, a wetting fluid displacing a non-wetting fluid, is called imbibition. As mentioned in section 2.2.1 there are major differences between drainage and imbibition, readily observed at the pore level. During drainage the displacement front will get stuck at the narrowest point in a pore, while during imbibition the non-wetting fluid will pull the front through the narrow points and get stuck at widest point in a pore. This effect is called capillary suction. Figure 2.3 illustrates the difference between the two processes.

Figure 2.3 illustrates the drainage and imbibition process during very slow displacement, where the capillary forces dominate the viscous forces. A detailed study of drainage and imbibition can be found in the a paper by Lenormad et. al. [23].

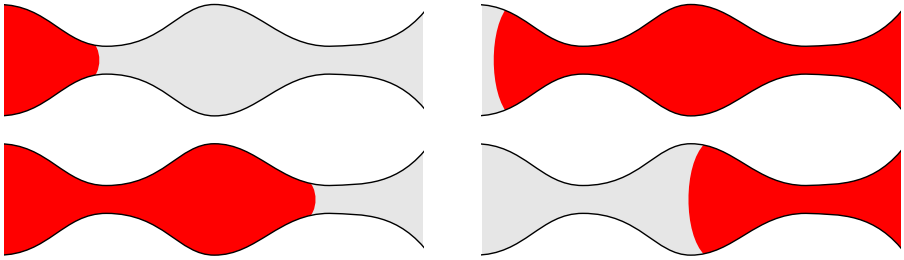

Figure 2.3: Drainage (left) and imbibition (right) in single pore. During drainage the non-wetting front gets stuck at a narrow point in the pore as the surface tension balance the pressure gradient. As the gradient overcomes the interface tension the front moves until the interface tension once again balances the pressure gradient, at the next narrow throat. During imbibition the forces balance at the widest point of the pore and gets sucked through the narrow throats.

2.3.2 Transient flow in porous media

The invasion phase of multiphase flow in porous media has been studied by several independent groups both experimentally and numerically. These groups have largely concerned themselves with situations where one fluid inhabits the porous media, while another is injected into the network. This means that only the invasion phase of the flow has been studied as the experiments are complete when the invasion front reaches the end of the media. This situation must by now be considered well understood with different flow regimes being identified depending on the capillary number, the viscosity ratio and the displacement mechanism. Furthermore the different flow regimes have been found to be well modelled by various geometric models. The low Ca regime known as capillary fingering has been found to behave as invasion percolation [13, 25, 43], viscous fingering can be modelled by diffusion limited aggregation [12, 30, 34, 44] and stable displacement can be modelled by anti diffusion limited aggregation [24,34]. The algorithms of each of these geometrical models are presented in appendix E. Figure 2.4 show the various invasion regimes from 2 dimensional invasion experiments.

Lenormand et. al. produced a phase diagram displaying the relation between the capillary number, the viscosity ratio and the identified flow

regimes [24]. The phase diagram is displayed in figure 2.5. Note that in the phase diagram the viscosity ratio is defined as the ratio between the viscosity of the defending and the invading fluid.

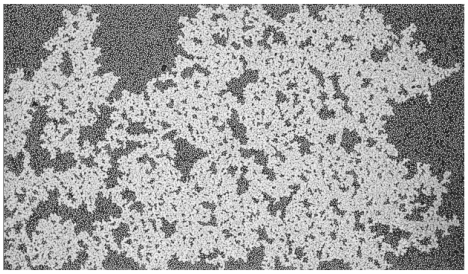

(a) Capillary fingering

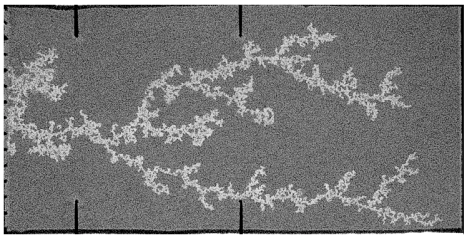

(b) Viscous fingering

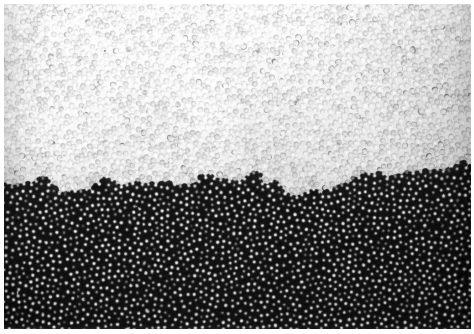

(c) Stable displacement

Figure 2.4: Different invasion regimes. All figures from Tallakstad [39]

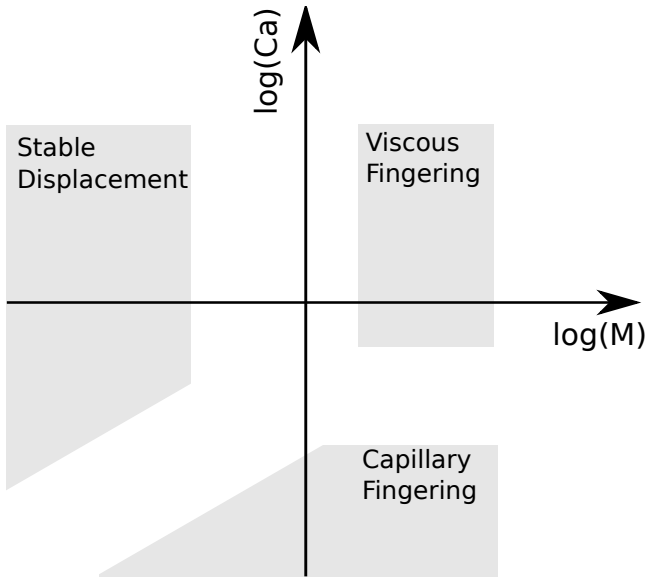

Figure 2.5: The flow regime phase diagram of Lenormand et. al. [24]

2.3.3 Steady state flow in porous media

During the invasion phase with a single injected fluid the system exhibits one continuous invasion front. The flow can be characterised as either imbibition or drainage depending on whether the non-wetting fluid is the defending or the invading fluid. When injecting both fluids simultaneously the displacement structure is significantly altered from the fronts shown in figure 2.4. The continuous invasion front is replaced by a highly fragmented invasion structure, and the defending fluid is no longer displaced by a continuous stream of invading fluid but rather by multiple small invasion clusters. Figure 2.6 shows an image of the invasion process with simultaneous injected fluids. An invasion front is still visible, but it is fragmented and not as clearly defined as the single fluid injection invasion fronts displayed in figure 2.4.

As the invasion clusters move across the porous they can get trapped in the medium, merge with other clusters, split into smaller clusters or get deformed in various ways. This leads to continuously changing flow conditions. The described fragmentation is caused by the background flow field of the wetting phase during simultaneous injection. As the invasion cluster of non-wetting fluid extends into the medium, imbibition will occur somewhere behind the invasion front. This will disconnect the invasion front from the injection point and create a so called invasion cluster. This new invasion cluster is also vulnerable to splitting by imbibition, leading to further fragmentation. The degree of fragmentation depends on the flow rate, viscosities and relative permeabilities of the injected fluids. The existence of these clusters lead to complicated flow patterns as clusters get stuck, split and merge.

Sometime after the invasion front has reached the end of the porous media the steady state is reached. During steady state flow the wetting phase saturation, pressure and non-wetting cluster size distribution remains constant if averaged over some time period [39].

The qualitative behaviour of the steady state flow depends on the capillary number, the viscosity ratio and the wetting fluid saturation. Payatake et. al. [6,7] identified different steady state flow regimes. The two regimes that are relevant with the parameters used in this thesis are called large ganglion dynamics and small ganglion dynamics. These two regimes are qualitatively very similar. In both cases the wetting fluid percolates the

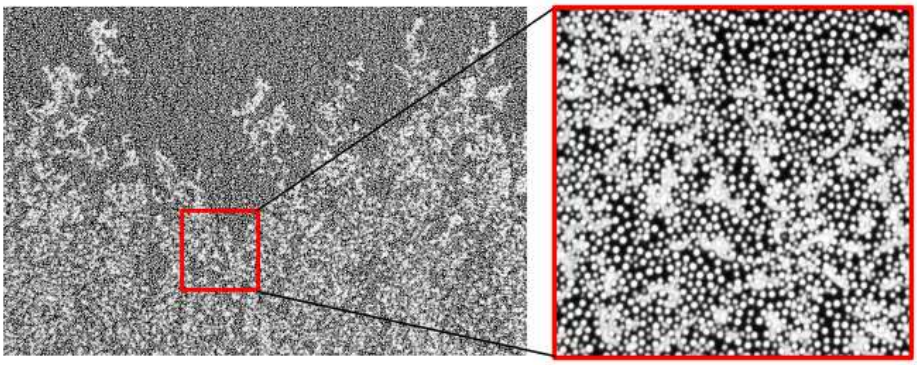

Figure 2.6: Invasion front from an experiment with simultaneously injected wetting (black coloured) and non-wetting (white coloured) fluid displacing the wetting fluid. The rectangle shows the fragmented invasion front. The small white circles are the glass beads that constitute the porous medium. Experiment performed at the Complex lab at the University of Oslo. Figure from Tallakstad [39].

medium through a continuously changing network of interconnected pathways, while the non wetting fluid exists as disconnected clusters. The clusters independently move through the medium where they can get trapped, split or merge with other clusters. The size of these clusters is what separates the two flow regimes. At small capillary numbers the average size of the cluster is an order of magnitude larger than the size of a single pore. This is known as large ganglion dynamics. As the capillary number increases and the wetting fluid saturation decreases the clusters become significantly smaller resulting in small ganglion dynamics. It should be emphasized that there is no sharp limit between these two flow regimes. Figure 2.7 shows a pore level image of a steady state flow experiment at the complex lab in Oslo, the disconnected non wetting clusters span multiple pores.

There is also a flow regime where both the non-wetting fluid and the wetting fluid percolate the medium. This is known as connected pathway flow. In this regime both phases flow through the medium in relatively stable independent pathways. This regime is observed at relatively large capillary numbers and small wetting phase saturation and will not occur

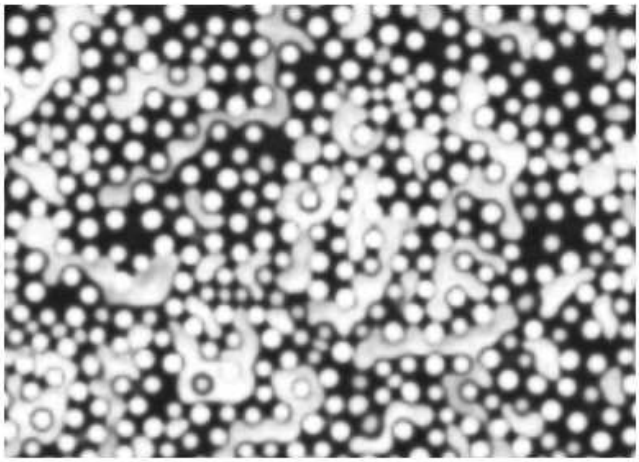

Figure 2.7: Close up of steady state flow experiment with $Ca = 1.5 \times 10^{-2}$ from the complex group in Oslo. The clusters of non-wetting fluid (white) are separated by a interconnected network of wetting fluid (black). The small white circles are the glass beads that make up the porous media. Figure from Tallakstad [39]

with the parameters used in this thesis, but it serves to emphasize the rich dynamics of steady state flow.

A thermodynamic state is a set of parameters that fully describe a thermodynamic system. Once these parameters are defined all other thermodynamic quantities can be calculated. Such a thermodynamic system is completely memoryless and is only dependent on the current values of the parameters. Multiphase flow in porous media is believed to be analogous to such a state where statistical properties such as cluster size distribution, non-wetting fluid saturation and pressure difference depend on the parameters viscosity ratio, capillary number and the wetting fluid injection fraction. In [15] Erpedling et. al. demonstrate that the statistical properties that characterise the steady state flow are history independent with respect to capillary number, further implying that steady state flow can be viewed as a true thermodynamic state.

2.3.4 Haines jumps

Two phase flow in porous media exhibit so called pinning-jumping behaviour or Haines jumps. These were first described by Haines during a study of water movement in soil [18]. In the case of drainage the effect can be described as an invading front getting trapped in a narrow pore because of the large capillary pressure at the interface. As the pressure behind the front keeps rising the interface pressure will be overcome and the front will be dislodged. The front will then surge forwards and the pressure will drop until it again reaches a pore narrow enough to again get stuck, repeating the process. This surge forward is called a Haines jump or a burst.

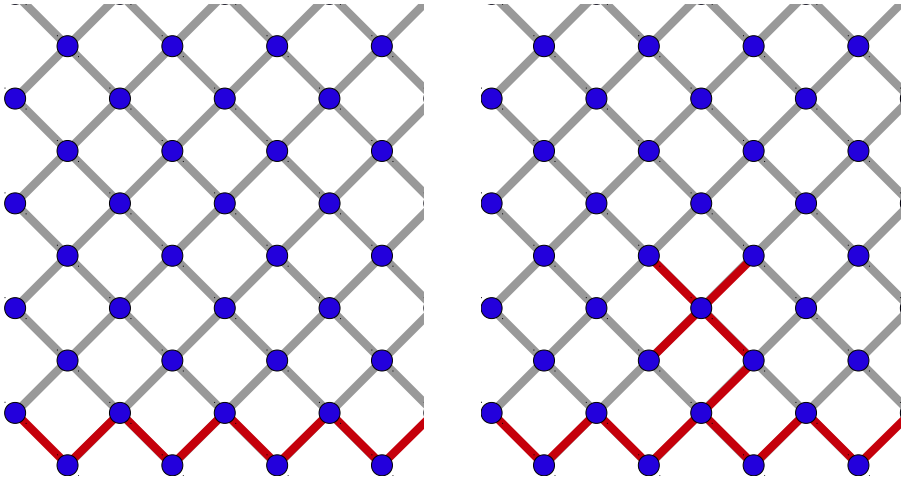

Figure 2.8: Fluid configuration before and after a burst during drainage in a network. The grey tubes are occupied by the wetting fluid while the red tubes are occupied by the non-wetting fluid. The geometric area of the invaded tubes defines the burst size

Figure 2.8 shows the fluid configuration immediately before and after a burst during the invasion phase. The invading non-wetting fluid is shown in red and the defending wetting fluid is shown in grey. The invading fluid is assumed to be injected into the bottom row from an exterior reservoir by a pressure difference across the lattice. The burst itself happens quickly with the fluid front moving orders of magnitude faster than the front

displacement velocity through the network [29]. Figure 2.8 shows that the invading fluid occupies five pores more after the burst than before the burst. The burst size s during an invasion is defined to be the geometric area invaded by the fluid during the burst. In this case the burst size would be the sum of the five invaded pores. During steady state flow there is no continuous invasion front and therefore the burst size definition used during the invasion phase is not applicable. The burst size is therefore defined as the area swept by a bubble during it's rapid displacement.

2.4 The correlation function

A correlation function describes the statistical correlation between random variables at different points in space or time. Given a random variable $X(\mathbf{x}, t)$ defined on some spatial domain and some temporal domain the correlation function is defined as:

$$G(\mathbf{x_1}, \mathbf{x_2}, t_1, t_2) = \text{corr}\left(X(\mathbf{x_1}, t_1), X(\mathbf{x_2}, t_2)\right) \tag{2.17}$$

where corr is the statistical correlation defined as:

$$\text{corr}(X, Y) = \frac{E\left[(X - \mu_X)(Y - \mu_Y)\right]}{\sigma_X \sigma_Y} \tag{2.18}$$

here E is the expected value operator and μ_X and σ_X are the expected value and standard deviation of the random variable X. Correlation is often assumed to be independent of absolute positions and times and only dependent on the difference. This assumption has been made in this thesis, resulting in a final correlation function:

$$G(\Delta\mathbf{x}, \Delta t) = \text{corr}\left(X(\mathbf{x}, t), X(\mathbf{x} + \mathbf{\Delta x}, t + \Delta t)\right) \tag{2.19}$$

The temporal correlation in a single point, $\Delta x = 0$, is usually referred to as the autocorrelation. While the spatial correlation between two points is referred to as the two point correlation.

2.5 Self organized criticality and power laws

Self organized criticality is a property of systems which have a critical point as an attractor. In their 1987 paper Bak et al. claim that the $1/f$

spectra reflects the dynamics of a self organized critical state of minimally stable clusters of all length scales, which in turn generates fluctuations on all length scales [8]. This was met with considerable interest as the $1/f$ spectra frequently occurs in nature, and self organized criticality could reproduce the spectra as an emergent phenomenon, without the tuning of control parameters.

In their paper the authors also presented the now famous example of a sand pile constructed by the continuous pouring of sand. In a cellular automation model they demonstrated that such a pile will quickly obtain some stable slope. A sand pile with this slope is said to be in it's minimally stable state. All perturbations to a system in a minimally stable state will result in fluctuations around the stable state. These fluctuations occur on all relevant size scales. In the specific case of a sand pile a perturbation would be adding more sand to the top of the pile, which will induce avalanches of various sizes. The frequency and size of the avalanche, $f(s)$, then follows the scaling relation $f(s) \propto s^{-\tau}$. This type of scaling relation is called a power law.

Frette et. al. demonstrated a power law experimentally in a pile of rice. However they also showed that self organized criticality is not universal and completely independent of system details, as the avalanche size distribution depends on the shape of the rice. Avalanches in a pile of short rice follow a stretched exponential distribution, while more elongated rice displayed a power law distribution [16].

Power laws have two properties that make them interesting. Primarily the property of scale invariance. Scale invariance means that scaling the argument by some factor c results in a proportional scaling of the function itself. That is,

$$\begin{aligned} f(x) &= ax^k \\ f(cx) &= a(cx)^k \\ f(cx) &= ac^k x^k \\ f(cx) &= c^k f(x) \end{aligned}$$

scaling the argument by c is equivalent to scaling the function itself with c^k. The exponent k is called the critical exponent of the power law.

Scale invariance means that all power laws with the same exponent are equivalent except for some constant scaling factor. This implies the second property of universality. Diverse systems with the same exponent have been shown to share the same fundamental dynamics. Such systems are therefore said to belong to the same universality class.

3 Method

3.1 The network model

The model used is based on the one presented by Aker et. al. in reference [3] and [4]. We will here explain the original model, and how the model used in this thesis differs.

The porous medium is modelled as a two-dimensional lattice of tubes oriented at 45° relative to the lattice edges. All the tubes have the same length d, but each tube's radius r is drawn randomly from a uniform distribution such that $r_{\min} \leq r \leq r_{\max}$ and $r_{\min} < r_{\max} < d$. These random radii are used to model the irregular structures usually present in a porous medium. An intersection of tubes is called a node. These nodes are assigned no volume, meaning that all fluid is contained in the tubes.

The fluids are assumed to be incompressible and immiscible. The immiscibility means that the fluids form menisci where they meet, and flow through the lattice as bubbles. All bubbles are assumed to extend along the full width of the tubes. This means that within a tube the flow is one-dimensional.

The capillary pressure across a meniscus acts as if the tubes were hourglass shaped. By assuming the principal radii of curvature of the meniscus is equal to the radius of the tube and that the wetting fluid perfectly wets the medium, the following relation can be derived using the Young-Laplace law:

$$p_c = \frac{2\gamma}{r}\left[1 - \cos\left(\frac{2\pi x}{d}\right)\right] \tag{3.1}$$

Here γ is the surface tension and d denotes the length of the tube. By letting the capillary pressure follow this relation small displacements of the interface within the tube can be accounted for. These effects are important for burst dynamics [17,31]. Figure 3.1 shows a single tube with a single bubble. It illustrates how the hourglass shape is used to calculate the interface pressure while flow rate is calculated under the assumption that the tube is circular and of constant radius.

The flow between two nodes i and j, q_{ij}, is solved using Hagen-Poiseuille flow in a cylindrical tube and Washburn's approximation [42], see section 2.2.1, resulting in the following equation:

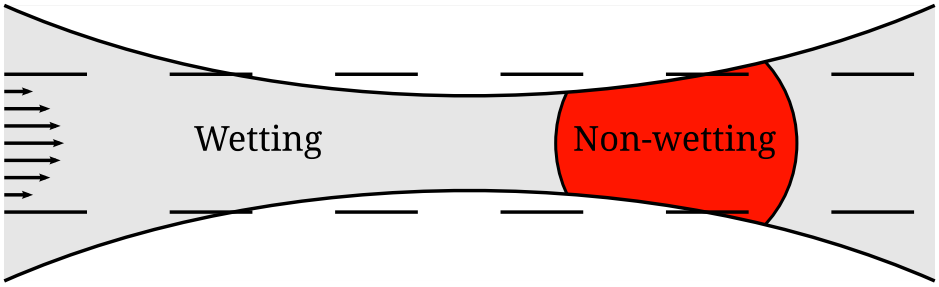

Figure 3.1: A single tube in the network. The flow rate is obtained by considering a circular tube while the capillary pressures are calculated by considering an hour glass shape.

$$q_{ij} = \frac{-\sigma_{ij} k_{ij}}{\mu_{ij}} \left(\frac{p_i - p_j - p_{ij}^c}{d} \right) \tag{3.2}$$

Here σ_{ij} and k_{ij} denotes the cross section and the permeability of the tube respectively. The subscript ij implies the tube between node i and node j. The effective viscosity within a tube is denoted μ_{ij}, this is the average viscosity weighted by the amount of each fluid in the tube. The p_{ij}^c term is the total capillary pressure contribution in the tube. That is the sum over all interfaces in the tube, with each capillary contribution calculated by equation 3.1. As the nodes contain no volume, the net flow in and out of every node must be zero. This statement is equivalent to Kirchoff's current law in a resistor network. Kirchoff's current law applied to the flow is given by

$$\sum_j q_{ij} = 0 \tag{3.3}$$

Inserting equation 3.2 into equation 3.3 results in an equation of the form

$$\sum_j \frac{-\sigma_{ij} k_{ij}}{\mu_{ij}} \left(\frac{p_j - p_i - p_{ij}^c}{d} \right) = 0 \tag{3.4}$$

This is a linear equation set for the flow through a single node, using

standard matrix notation the equation set becomes:

$$D_{ij}p_j = B_i \tag{3.5}$$

Where the matrix D_{ij} is the conductivity matrix, and the vector B_i contains the capillary pressures, p_{ij}^c. This equation set can be solved given some set of boundary conditions. This is where the two models diverge.

In the original model periodic boundary conditions are applied in both the horizontal and vertical direction and ghost nodes are introduced at the boundary to enforce a pressure drop across the lattice. To ensure a constant flow rate Q the system must be solved twice with two different pressure drops across the lattice. This model produces excellent results, however the periodicity in the flow direction is quite far removed from physical experiments. To amend this the model was altered slightly.

In the altered version periodic boundary conditions were used in the horizontal direction, however the vertical periodicity was removed in favour of simultaneous injection of both fluids into nodes along the bottom row. The top row was held at constant pressure and any fluid moving beyond this row was removed from the system. With these boundary conditions the system was solved for p_j using the Conjugate-Gradient Method detailed in appendix B. The injected fluid along the bottom is accounted for as an additional term in the B_i vector so equation 3.5 is altered to:

$$D_{ij}p_j = B_i' \tag{3.6}$$

Where B_i' contains both the fluid injection and the total capillary pressures in the tubes. The full conductivity matrix and capillary pressure vector for a small system is presented in appendix C. After solving equation 3.6 for the pressure in each node, the menisci are moved resulting in a new B_i' vector and a new D_{ij} matrix.

The bubbles are moved in accordance with the following experimentally motivated rules:

- Within a single tube the bubbles are moved a distance determined by equation 3.2.
- There can be maximum n bubbles in each tube. If there are more than n bubbles, then the two bubbles which are closest to each other are merged.

- If two bubbles are closer than some distance $d_{\min}$ they are merged.
- At each time step the total volume and non-wetting volume flowing through all nodes is calculated. New bubbles are formed upstream from the node.
- When creating new bubbles the non-wetting fluid is distributed equally in the upstream tubes.
- When creating new bubbles the position of the non-wetting bubble alternates between the beginning of the tube and directly after the wetting fluid.

When merging and creating new bubbles both non-wetting and wetting volume is conserved.

More details about the precise movement of the menisci can be found in [3] and [4]. A thorough discussion of the model can also be found in the thesis of Evind Aker, along with comparisons between the model and experimental results [2].

An illustration of the lower part of the network with the injection nodes is shown in figure 3.6.

3.2 Finding the start of the steady state

As mentioned in section 2.3.3 steady state is reached sometime after the invasion front reaches the top of the lattice. This point is usually referred to as breakthrough. Thereby every point in the lattice will reach steady state simultaneously. Figure 3.2 shows the pressure development at several nodes in the the lattice during a simulation.

From figure 3.2 it is evident that every point reaches steady state simultaneously. The start of the steady state phase for the entire lattice can thereby be defined from the pressure measurements of any node. Steady state is defined to begin the first time the following relation holds:

$$p_i^{t_{\text{start}}} \geq p_{\text{ref}} \tag{3.7}$$

where p_i^t is the pressure reading at node i at time t, and the reference pressure, p_{ref}, is the average pressure of the final 10% of pressure measurements for this particular node. This should give the time of the start

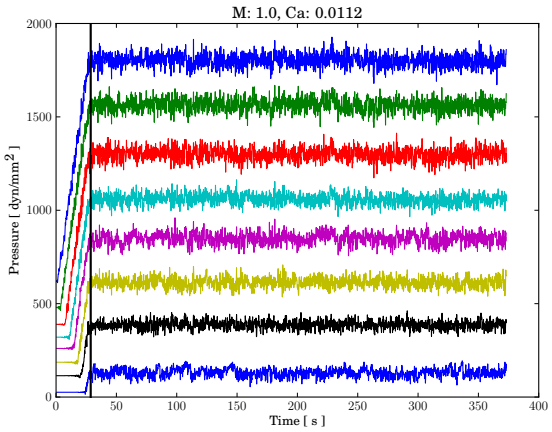

Figure 3.2: Pressure development at several points in the lattice during a simulation with viscosity matched fluids and $Ca = 11.2 \cdot 10^{-3}$. Every point reaches steady state simultaneously.

of the steady state for the entire system by sampling any point on lattice, however large bursts at the end of the invasion period could significantly skew the result. Therefore the entire lattice is sampled and the entire system is said to have reached steady state when 90% of all nodes have reached steady state as defined by equation 3.7.

3.3 Mixing length

When the fluids are injected into the bottom of the network they are in a completely unmixed state. The fluids will gradually be mixed together as they flow through the network until they reach a fully mixed state with no trace of the initial separate flow. The distance from the outlet where the fluids reach this state is defined as the mixing length l_{mix}. The flow through the nodes with $y < l_{\text{mix}}$ is not a properly mixed steady state flow and can not be expected to exhibit the same flow characteristics as the flow further downstream in the network. This includes the pressure evolution, and these nodes should therefore not be included in any statistical analysis of the pressure behaviour. Figure 3.3 shows two snapshots of the flow close to the inlet and further downstream to illustrate the mixing length effect.

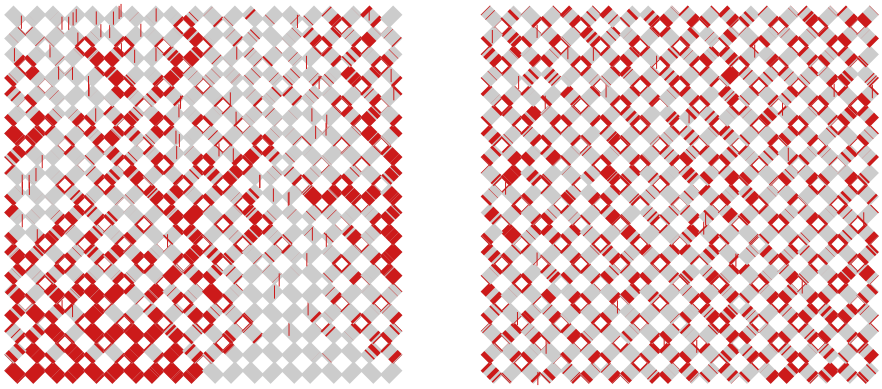

Figure 3.3: Nodes close to (left) and far from (right) the injection nodes. The fluids are not properly mixed close to the injection row.

Finding the mixing length is an unsolved problem. Various techniques were proposed for the purpose of this thesis however none were found to be satisfactory. The mixing length is therefore arbitrarily set to $l_{\text{mix}} = y_{\text{max}}/2$ in all data analysis. This reduces the number of valid data points enormously, but the flow through the remaining nodes can safely assumed to be in a properly mixed steady state.

3.4 Defining a burst

Section 2.3.4 describes the pinning-jumping behaviour of the flow in terms of geometric parameters. However it is difficult to measure the invaded area s directly. Therefore the burst size is inferred from pressure measurements, as the pressure will drop when the fluid surges forwards. Figure 3.4 shows part of a pressure-time series with a burst and relevant parameters.

A burst is defined to start whenever the pressure drops and lasts until the pressure exceeds the pressure at the beginning of the burst. Consecutive pressure drops are not counted as multiple bursts.

The geometric burst size s is inferred through the valley size, which is defined as:

$$\chi = \sum_i \Delta p_i \tag{3.8}$$

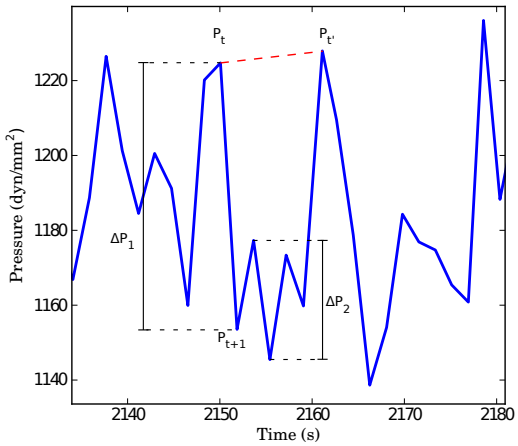

Figure 3.4: The burst starts at time step t and ends at time step t'. The first time step after the start of the burst is $t+1$. ΔP_1 and ΔP_2 are the first 2 contributions to the valley size χ.

Where Δp_i is the pressure drop between two consecutive data points. This definition is motivated by experimental work by Furuberg et. al. [17]. For low injection rates the following relation holds [17]:

$$\Delta\chi \propto s \tag{3.9}$$

meaning that the valley size distribution scales the same way as the burst size distribution.

This definition of a burst gives the option of allowing burst within burst (inclusive) or not allowing bursts within bursts (exclusive). In the paper by Aker et. al. [5] where the critical exponent of the bursts size distribution during slow drainage was studied the inclusive model was used. However not allowing bursts within bursts is also of interest as it is closely related to the breaking of a fibre bunch which has been studied by Hemmer and Hansen [19]. Therefore both analysis have been performed here. The two cases are illustrated in figure 3.5.

When not allowing bursts within bursts the maximum value of the pressure in a time series will mark the start of a burst that will never end.

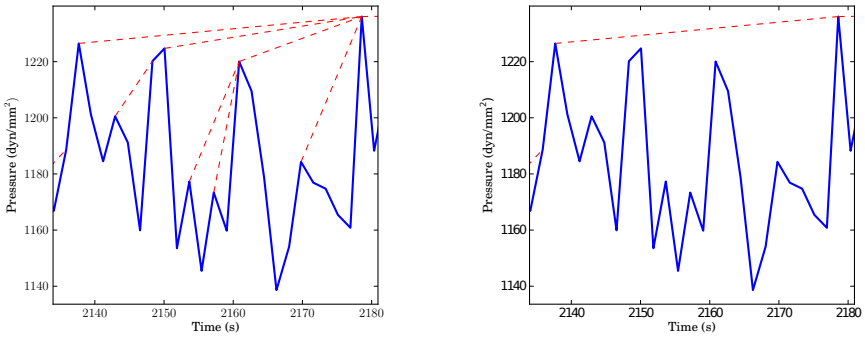

Figure 3.5: Burst when including bursts within bursts (left) and when excluding bursts within bursts(right)

This means that collecting exclusive burst data during the steady state is difficult without compromising the results by, for instance, selecting an area with no large pressure peaks. Therefore the exclusive analysis has only been performed on the transient pressure evolution.

When allowing bursts within bursts the maximum value will also start a burst which will never end, therefore any bursts that are ongoing at the last time step are not counted. This method still leaves the more general problem with other large peaks that may result in very large valley sizes, clearly disconnected from the geometric burst size, s. These bursts will slightly influence the final results, however because these events are rare their impact on the statistical distribution is small.

3.5 Finding the burst size distribution

The scaling relation of the burst size distribution is found from the χ distribution. As a power law is assumed the distribution of χ is found by sampling each event and then constructing a histogram of the distribution. The critical exponent is then found from linear regression of the reverse cumulative histogram in a log-log plot. The slope of the linear fit is the

critical exponent of the power law. This can be seen as

$$f(x) = cx^k$$
$$\log f(x) = \log c + k \log x$$

where k is the critical exponent of the power law and the slope of the best linear fit.

Logarithmic binning is used to construct the histogram. This is necessary as the difference in frequency between small and large events can be several orders of magnitude, resulting in multiple empty bins and consequently an inaccurate result if constant width bins are used. Logarithmic binning introduces and offset of +1 to the critical exponent after the regression, this is shown in appendix D.

3.6 Simulation parameters

All simulations were run on a 50×100 grid, with 10 injection points for each fluid along the bottom row. Despite the number of injection points the non-wetting fluid constituted only 40% of the total injected fluid. The interface tension was set to $\gamma = 3\,\mathrm{dyn/mm^2}$ in all simulations while the maximum number of bubbles in a single tube was set to 3 in all simulations. The tubes length was set to $d = 1.0\,\mathrm{mm}$, while the minimum distance between bubbles was set to $d_{\min} = 1.0 \times 10^{-12}\mathrm{mm}$. The tubes had a minimum radius $r_{\min} = 0.1\,\mathrm{mm}$ and a maximum radius $r_{\max} = 0.4\,\mathrm{mm}$. Each simulation was run for 200000 time steps, while sampling every 100 time steps. This is sufficiently long for the system to reach steady state and to stay in steady state long enough for data to be collected. All constant value simulation parameters are summarized in table 1.

Each simulation was run with a lattice initialized with the wetting fluid and alternating injection points for the wetting and the non-wetting fluid along the bottom row. Figure 3.6 shows the initial and injection row boundary conditions of the network. Note that for illustrative purposes the displayed network has more injection points than the network actually used in the simulation.

Simulations were run with capillary numbers in the range $Ca = 1.6 \times 10^{-3}$ – 14.6×10^{-3}, and with the viscosity ratio $M = 0.1, 1, 10$. Simulations far outside this range is difficult as the system takes very long to

Parameter	Value
Nodes per row	50
Number of rows	100
Injection points	10
$r_{\min}$	0.1 mm
$r_{\max}$	0.4 mm
d	1.0 mm
γ	3.0 dyn/mm^2
F	0.4
n	3
$d_{\min}$	1.0×10^{-12} mm
T	200000
D	100

Table 1: Simulation parameters. The minimum distance between bubbles is $d_{\min}$, d is the tube length, $r_{\min}$ and $r_{\max}$ is the minimum and maximum tube radius respectively. T is the total number of time steps and D is the number of time steps between each sampling. F is the non wetting fraction of the injected fluid.

Figure 3.6: The initial and boundary conditions for the bottom rows of nodes. The non-wetting liquid is shown in red while the wetting liquid is shown in grey. The entire lattice is initially filled with wetting fluid while wetting and non-wetting fluid is injected simultaneously.

reach steady state for low Ca while high values of Ca may break central assumption by increasing the impact of the dynamic wetting angle [11], which is unaccounted for, and introducing turbulence in the system if the capillary number is increased sufficiently. High capillary number will also result in a very short invasion phase which will not generate enough data for the exclusive burst size analysis. For low capillary numbers invasion event will frequently only involve a single tube. Such events are not expected to follow the same distribution as the multi pore invasions studied in this thesis. In fact Lehmann et. al. showed that the burst size distribution of low Ca single tube invasions is a power law, and that the critical exponent depends on the capillary number [22].

The injection rate is determined from the capillary number using equation 3.1. With the cross section area A determined by summing the area of all links and then diving by the number of rows, in this case 100.

A single simulation was run on a 50×200 network with $Ca = 3.2 \cdot 10^{-3}$ and viscosity matched fluids. This data was used to asses the impact of boundary effects on the flow.

4 Results and discussion

In this section results of all simulations are presented. Each result is discussed in term, while the errors and uncertainties are discussed at the end of the section.

4.1 Steady state inclusive burst size distribution

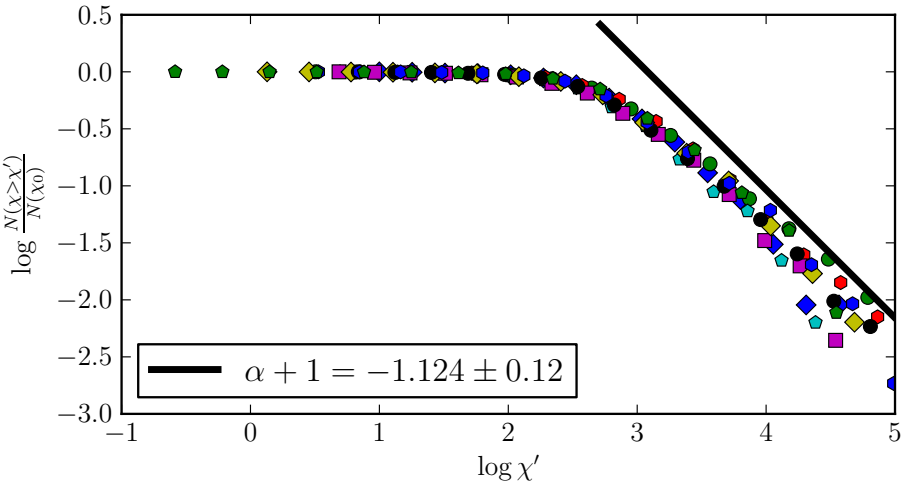

Figure 4.1: Steady state inclusive burst size distribution for $M = 10.0$ and all values of Ca, with best fitting straight line.

Figures 4.1, 4.2 and 4.3 shows the steady state burst size distribution for each value of M and all values of Ca with the best fitting straight line. Figure 4.4 show the burst size distribution for all M and all Ca with the best fitting straight line. Each of the different symbols in the figures represent a simulation with a specific value of Ca and M. All figures are log-log plots of the normalized reverse cumulative valley size distribution, χ. All distribution are good matches with a power law with critical exponents $\alpha \approx 2$. This law appears to be independent of the capillary number. It seems to apply to bursts larger than some threshold and stay valid for several orders of magnitude. The threshold exists as small events frequently only involve invasion of a single tube. These events

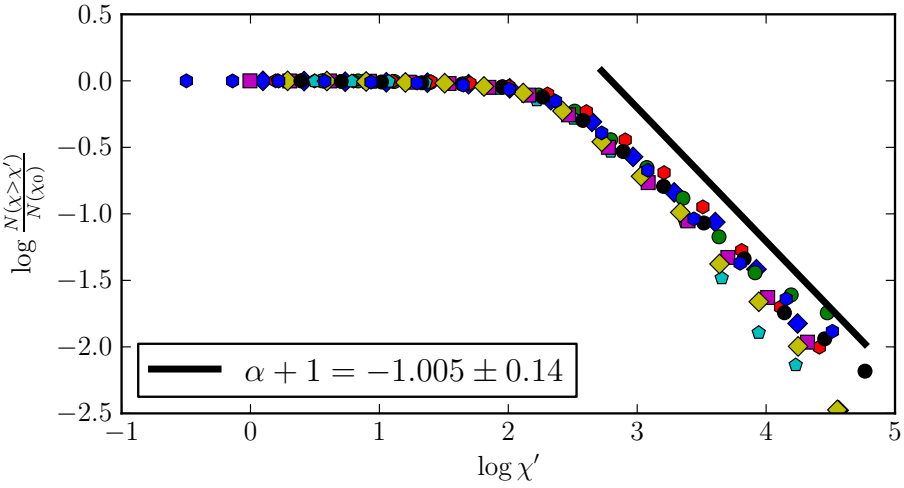

Figure 4.2: Steady state inclusive burst size distribution for $M = 1.0$ and all values of Ca, with best fitting straight line.

do not follow the same power law as the larger multi pore invasion events. The results are summarized in table 2.

Figure 4.5 shows the data from table 2. Together with figure 4.4 it shows that the exclusive burst size distribution follows a power law with a critical exponent $\alpha = -2.034 \pm 0.13$, and that this power law is independent of viscosity ratio as well as capillary number.

This result is consistent with the result found by Aker et. al. [5] for the inclusive burst size distribution during drainage. Aker et. al. noted that the results put drainage in the same sueruniversality class as invasion percolation, which was solved by Maslov [27] to have a critical exponent $\alpha = 2$. This result was expected for slow drainage which can be mapped directly to invasion percolation, however it is interesting that other invasion modes with no obvious mapping to invasion percolation also fall into this superuniversality class. Extending this line of though it is even more remarkable that steady state flow also falls into this superuniversality class considering how distinctly different it is from the invasion percolation process.

It interesting in itself that the power law scales the same way during

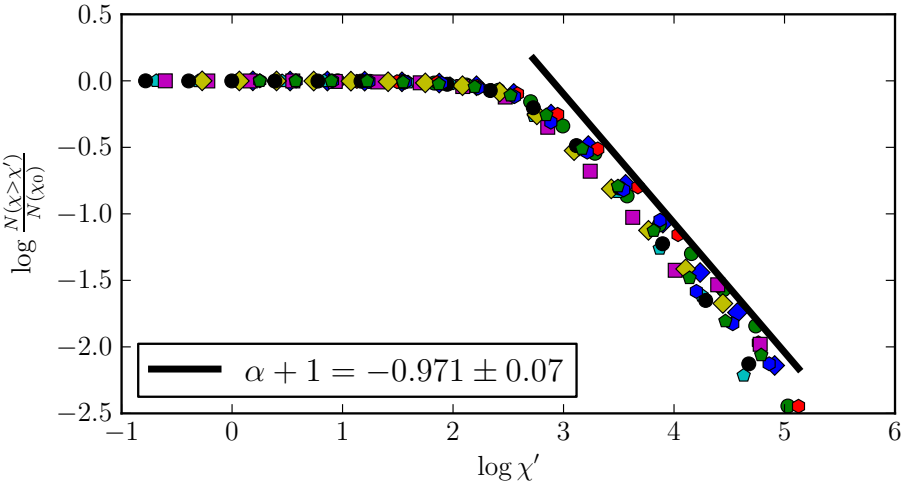

Figure 4.3: Steady state inclusive burst size distribution for $M = 0.1$ and all values of Ca, with best fitting straight line.

the invasion phase and the steady state phase. It should be noted that in the analysis of the bursts Aker et. al. corrected for the average drift of the pressure at large injection rates. It is nonetheless notable that the power law remains even with drastically different flow conditions and flow patterns.

Tallakstad found that the non-wetting cluster size distribution during steady state flow does depend on the capillary number [39]. This result was obtained experimentally with a system very similar to the one simulated in this thesis. This shows that the burst size distribution is independent of the cluster size distribution. This is notable as the cluster size distribution influences the total interface length between the two fluids and therefore should intuitively influence both the burst sizes and the burst frequencies.

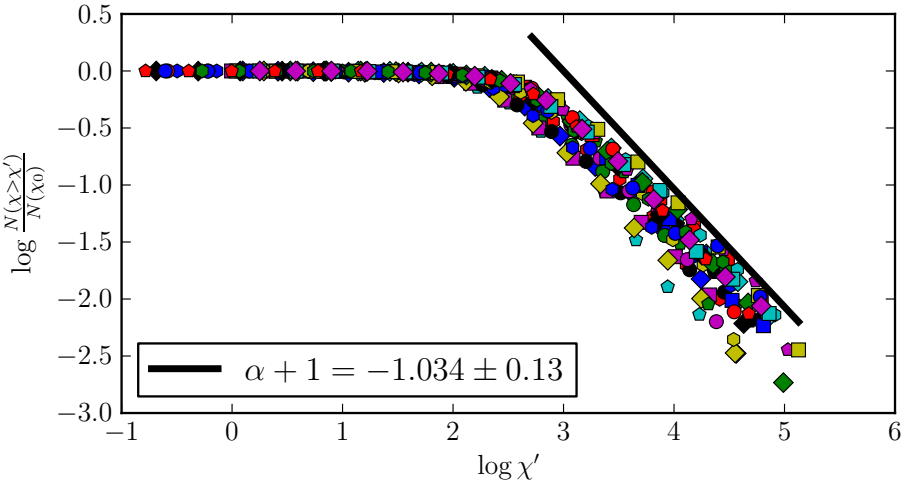

Figure 4.4: Steady state inclusive burst size distribution for all values of M and Ca, with best fitting straight line.

M	α
0.1	-2.124 ± 0.12
1.0	-2.005 ± 0.14
10.0	-1.977 ± 0.07
All	-2.034 ± 0.13

Table 2: Critical exponents, α, of the burst size distribution for each value of M. Acquired from linear regression on log-log plots of the steady state exclusive burst sizes.

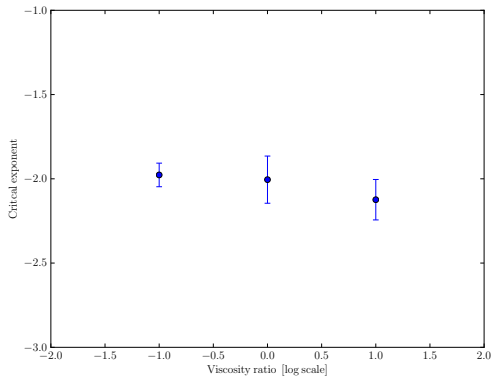

Figure 4.5: Plot of $\log M$ versus α. Two orders of magnitude reveal no statistical significant change in critical exponent and indicate that burst size distribution is independent of the viscosity ratio.

4.2 Transient exclusive burst size distribution

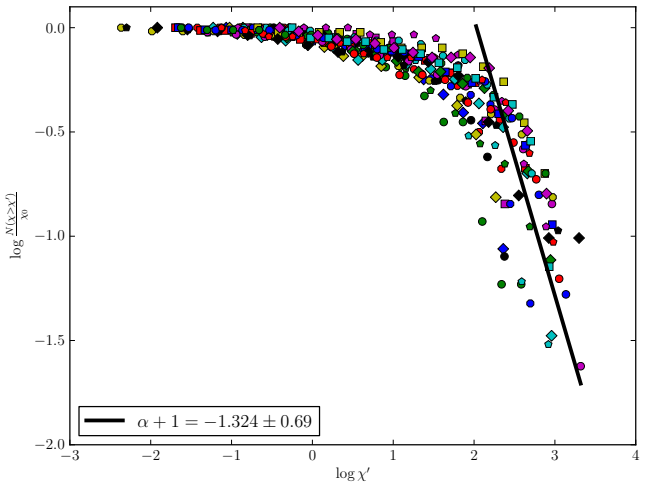

Figure 4.6: Transient exclusive burst size distribution for all values of M and Ca, with best fitting straight line.

Figure 4.6 shows exclusive burst size distribution for the transient for all values of M and Ca. The data appears qualitatively similar to the inclusive steady state distribution, however the variance in measurements is far larger, as reflected by the huge uncertainty in the best fitting straight line.

As the the duration of the invasion phase depends on the flow rate there is significantly less data for higher values of Ca. Therefore a plot was made only including simulations where $Ca \leq 4.8 \cdot 10^{-3}$. The result is displayed in figure 4.7. The best linear fit in this plot does have slightly smaller uncertainty, however the uncertainty is still far larger than the uncertainty in the steady state distribution. Plotting the data for a single value of M did not significantly reduce the uncertainty either.

It is obvious that the uncertainty in the result is far too large for any conclusions to be drawn. It is possible that the scattered data would collapse onto a single line like the steady state data if more data points were collected. This could be done either by increasing the length of the system thereby increasing the time it takes to reach steady state or by

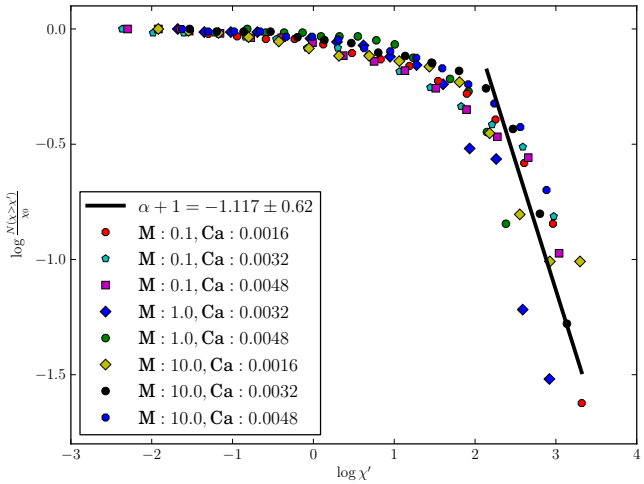

Figure 4.7: Transient exclusive burst size distribution with $Ca \leq 4.8 \cdot 10^{-3}$ and all values of M, with best fitting straight line.

simulating a smaller system multiple times and changing the radius of the links between each run.

Despite the large uncertainty in the result there are two interesting possibilities within the uncertainty range that should be considered. These are:

- The critical exponent is 2.5.
- The critical exponent is 2.0.

In the first case, $\alpha = 2.5$, the burst size distribution is identical to the one found for the fibre bunch model by Hemmer. et. al. [19]. In this paper the exclusive burst size distribution of bursts during the breaking of a fibre bunch was found to be a power law with critical exponent $\xi = 2.5$, while the inclusive burst size distribution was found to be a power law with critical exponent $\xi = 2$. These values were found to be universal and independent of the distribution of the strength of the individual fibres. Aker et. al. have found the inclusive burst size distribution during drainage to be a power law scaling as $\alpha = 1.9 \pm 0.1$, independent of Ca and M. This means that if the exclusive burst size distribution scales as $\alpha = 2.5$

two-phase flow perfectly mirrors the breaking of the fibre bunch model, despite the fact that two-phase flow is a significantly more complicated system.

In the second case, $\alpha = 2$, the burst size distribution is identical for inclusive and exclusive bursts in the transient. This would be an interesting result as it reveals the two-phase flow bursts to be fundamentally different from the fibre bunch bursts, despite some qualitative similarities. From a mathematical perspective it would be interesting as the exclusive burst size distribution is a subset of the inclusive burst size distribution. If the distributions are equivalent then sampling all exclusive bursts is an unbiased sample of the set of all bursts. Such an unbiased sample must usually be obtained by a random sampling of the set [21].

4.3 Spatial pressure variation

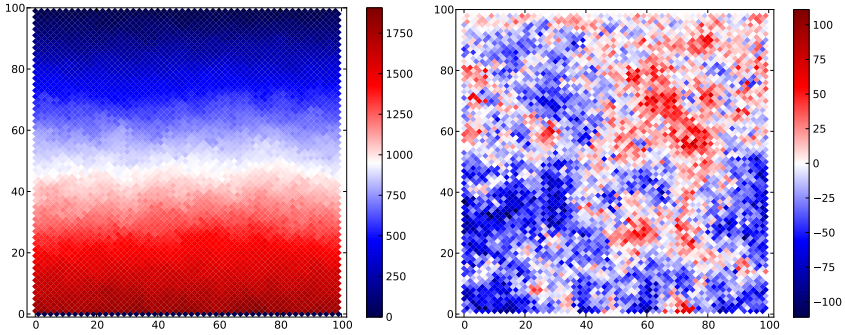

(a) Lattice pressure during steady state flow in units of dyn/mm^2.

(b) Lattice pressure during steady state with linear component subtracted in units of dyn/mm^2.

Figure 4.8: Lattice pressure during steady state flow. The main contribution comes from the linear pressure drop from the inlet. This component is removed in the plot to the right.

Figure 4.8 displays the pressure at every node in the lattice during steady state flow. The figures are generated from data from a simulation with the parameters $M = 1$, $Ca = 11.2 \cdot 10^{-3}$. This choice was arbitrary as the pressure plots were qualitatively similar for all simulation parameters.

The main contribution to the pressure appears to be the linear drop from the inlet. This is consistent with Darcy's law. Subtracting this component gives figure 4.8b, which display spatial pressure fluctuations from the mean.

The average pressure drop from the inlet was found to be $p(y) = 1859.37 - 18.79y\,\mathrm{dyn/mm^2}$. The magnitude of the pressure drop depends on the flow parameters in accordance with Darcy's law, equation 2.9. It will in all cases fall linearly downstream from the inlet.

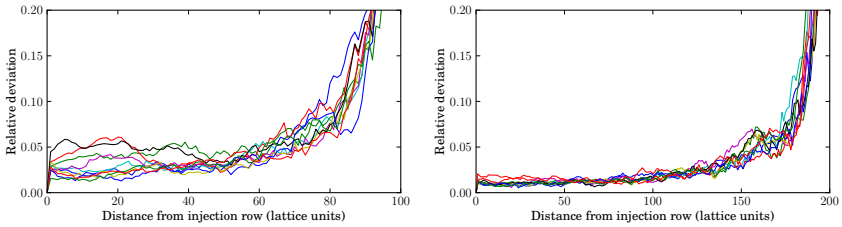

(a) Row averaged relative deviation from Darcy pressure. On a 50×100 lattice.

(b) Row averaged relative deviation from Darcy pressure. On a 50×200 lattice.

Figure 4.9: Row averaged relative deviation from the Darcy pressure. The absolute value of the deviation in each node was summed over each row. Each line represents a different time step.

Figure 4.9 shows the average relative deviation from the Darcy pressure. It is obtained by summing the absolute value of the deviation over each row, and plotting it against the distance from the inlet. This was done for several different time steps. The divergence at the outlet is caused by the zero pressure boundary condition enforced on the top row.

Inspection of figure 4.9a shows that the relative deviation from the Darcy pressure is approximately constant and small for the first 60 lattice units. The pressure deviation increases slowly between 60 and 80 lattice units and then diverges as it approaches the singularity at the outlet. Figure 4.9b shows the relative deviation on a much larger lattice. It reveals that the slow increase in the deviation observed before the divergence is also caused by proximity to the outlet, not by distance from the inlet. The relative deviation plot shows that not only the mixing length from the inlet, but also the distance from the outlet needs to be considered when

collecting data. Assuming a mixing length $l_{\text{mix}} = 50$ only a very limited number of nodes can be considered before boundary effects become large.

All data used for analysis in this thesis was collected from nodes in the range $y = 50$ to $y = 75$. We assume that the flow through theses nodes is a properly mixed steady state two phase flow not too heavily influenced by the boundary conditions.

4.4 Steady state correlation profiles

4.4.1 Autocorrelation

The following plots are autocorrelation plots of the pressure series of the point $(50, 50)$ from the simulation with $M = 0.1$ $Ca = 1.46 \cdot 10^{-2}$. This choice was arbitrary as all inspected autocorrelation plots were similar, both qualitatively and quantitatively.

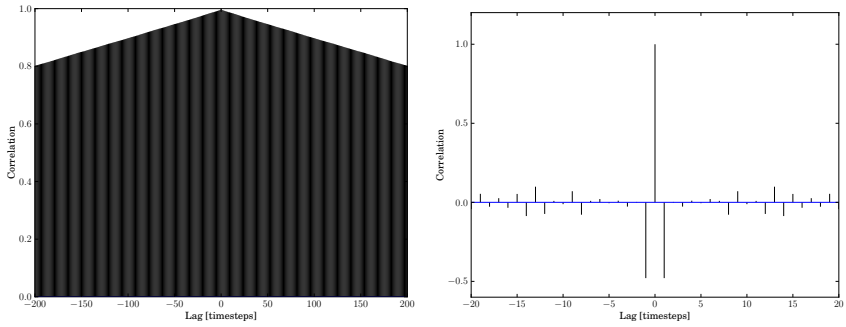

(a) Pressure signal autocorrelation. (b) Pressure change autocorrelation.

Figure 4.10: Autocorrelation of the pressure series (left) and the change in the pressure series(right). The autocorrelation of the pressure series decreases linearly while the pressure movement is negatively correlated for lag = 1, but seemingly uncorrelated for larger lags.

Figure 4.10 shows the autocorrelation of the pressure in the lattice and the autocorrelation of the change in pressure in the lattice. The triangular shape of the autocorrelation plot is indicative of an autoregressive process of the form:

$$x_t = c + \sum_{j<t} \alpha_{t-j} x_{t-j} + \epsilon \tag{4.1}$$

where ϵ is a random number drawn from some distribution. A wide range of processes fall into this class including the random walk which is an autoregressive process with $\alpha_{t-j} = 1$ for $j = 1$ and $\alpha_{t-j} = 0$ for $j \neq 1$. In other fields significant effort has been spent finding statistical methods for estimating all the factors α_{t-j} [26], often with the aim of trying to extrapolate future trends from a time series. No such statistical analysis will be attempted here, as the statistical future behaviour of the system is known.

The autocorrelation in the pressure changes, Δp, has also been computed. It is clear that the pressure change at time step t is negatively correlated with the previous one, at time step $t - 1$. This is not unexpected as the pressure of the system fluctuates around a stable value and any pressure change away from this value should, on average, be followed by a move back towards the stable level. It is surprising that there is no correlation for lag $= 2$ and lag $= 3$ as by the same argument one would expect decaying oscillations. This discrepancy could be caused by bursts as a large burst could result in consecutive pressure drops. This would also explain the reappearance of the sine like behaviour at larger lags as only the largest bursts exist on this time scale.

4.4.2 Spatial correlation

The following plots are spatial correlation plots from the pressure at different nodes in a simulation with $M = 1$ and $Ca = 11.2 \cdot 10^{-3}$. This choice is arbitrary as all inspected correlation plots were qualitatively similar.

Figure 4.11 shows the two point correlation from the point $50, 50$ and the average correlation in the lattice. The average correlation for a single node in figure 4.11b is computed by:

$$\langle corr_{x'y'} \rangle = \frac{1}{N-1} \sum_{x' \neq x} \sum_{y' \neq y} corr\left(P(x', y', t), P(x, y, t)\right) \tag{4.2}$$

where N is the total number of nodes in the network and *corr* is defined in equation 2.19. The figures show that the correlation decreases

with distance and that the correlation decreases faster in some directions than in others. Figure 4.12 and 4.14 shows how the correlation functions scales with distance and demonstrates the directional asymmetry present in figure 4.11.

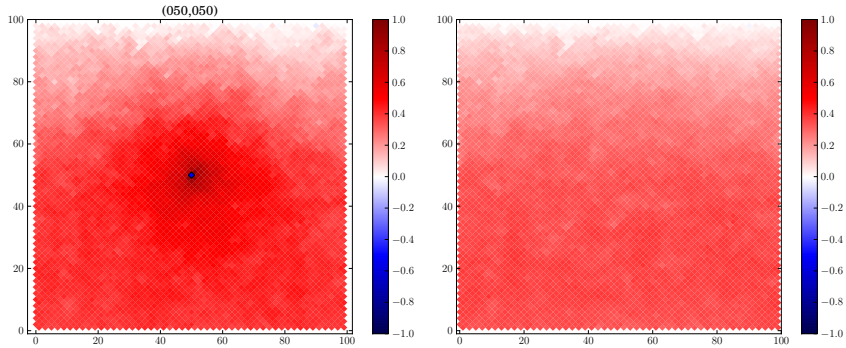

(a) Two point correlation between the point $(50, 50)$ (in blue) and all other points.

(b) Average correlation between all points.

Figure 4.11: Two point correlation map and average all points correlation map. The average plot represents the average correlation between each point and all other points.

Figure 4.12 displays the correlation as a function of distance. The sudden drop at around 50 lattice units is caused by the periodicity in the lattice. This is shown in figure 4.12b which shows the correlation as a function of distance when only considering the horizontal and vertical directions. It is also influenced by the fact that the average correlation falls downstream, as seen in figure 4.14.

The correlation as a function of distance fits well with a function of the form:

$$G(r) = \frac{1}{(ar+1)^{0.5}} \tag{4.3}$$

where the value a is a fitting parameter. Figure 4.13 shows the fitting parameter a as a function of capillary number. The value of a appears to depend on Ca in some non-linear manner while it appears to be independent of the viscosity ratio. For large values of r equation 4.3 approaches a power law with critical exponent $\eta = 0.5$. This scaling relation is similar

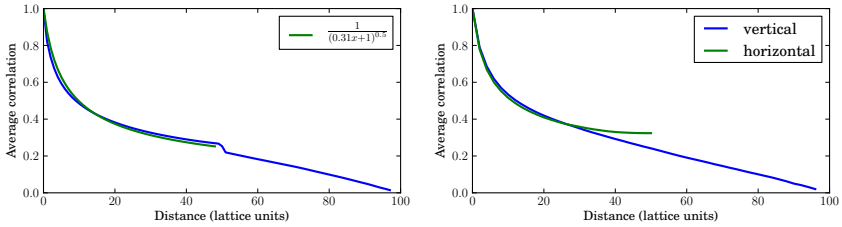

(a) Average two point correlation as a function of distance. The green curve is the best fitting function.

(b) Average correlation in the x and y direction as a function of distance.

Figure 4.12: The two point correlation coefficient as a function of distance. The plot to the right shows the correlation as a function of distance when only considering the y (up) and x (right) direction. The plot shows that the correlation in the x and y direction diverges slightly at large distances.

to the correlation function of a scale invariant scalar field, which in general scales as:

$$G(r) \propto \frac{1}{r^{D-2+\eta}} \tag{4.4}$$

where D is the dimension of the system, and η is some critical exponent. An example of a scale invariant scalar field is the two dimensional Ising model at the critical temperature, which has has a critical exponent $\eta = 1/4$ [28], giving a correlation function scaling relation:

$$G(r) \propto \frac{1}{r^{\frac{1}{4}}} \tag{4.5}$$

Comparing equation 4.3 and 4.5 reveals that the correlations in the pressure in the porous media decays significantly faster than the spin-spin correlations in the two dimensional Ising model.

Figure 4.14 shows the row-averaged correlation as a function of distance from the inlet. This is a measure of how correlated each row is with the rest of the network. It is interesting that the average correlation falls quickly as the distance from the inlet increases. Figure 4.14a shows that the average correlation in a 50×100 network decays quickly for distances larger than ≈ 50 lattice units. This distance is consistent with the start of the divergence from Darcy's law observed in figure 4.9a so the decay could

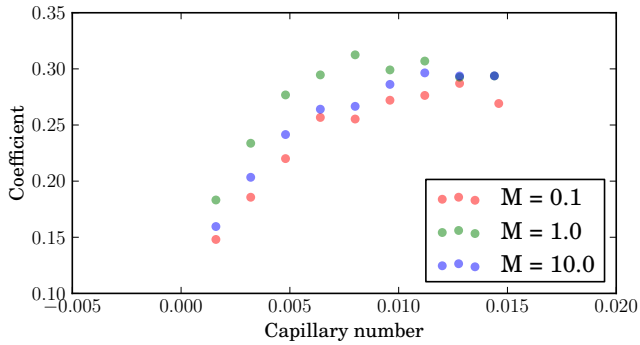

Figure 4.13: Curve fitting coefficient as a function of capillary number.

be caused by the boundary conditions on the top row. Comparison with figure 4.14b reveals this not to be the case as the average correlations in the much larger 200×100 also appears to start to decay about halfway through the network.

Figure 4.14b and 4.14a appear qualitatively similar except for the small increase in the beginning. This increase is interesting as it appears to be approximated 20 lattice units for both the small and the large network. It is possible that this distance could be used to defined the mixing length, however to verify this the cluster size, saturation and pressure needs to be thoroughly investigated. In any case it is a highly impracticable definition from a experimental perspective as it is infeasible to measure average correlation in an experimental set up.

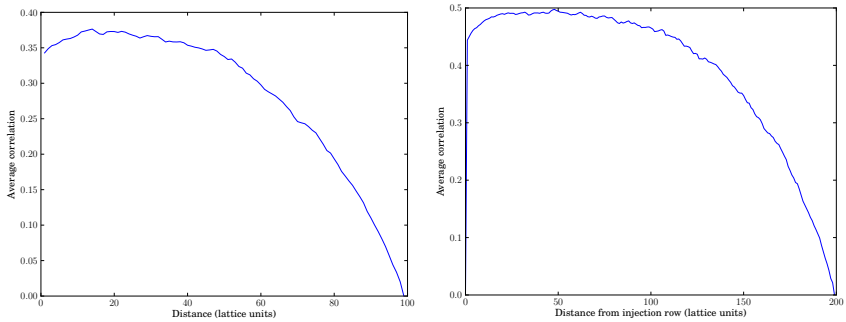

(a) Lattice size 50×100. (b) Lattice size 50×200.

Figure 4.14: Row-averaged average correlation coefficient as a function of distance from the inlet. The nodes closer to the inlet are more correlated to the system than the nodes far from the inlet.

4.5 Errors and uncertainties

There are several sources of errors and uncertainties both in the model and in the data analysis methods that we have used. In this section the most significant error sources are identified and discussed. We also present an explanation of the uncertainty in the critical exponent of the burst size distributions.

Model related error sources

The network model we used contains multiple simplifications. The most notable approximations are the assumption of perfect wettability, approximating the pores as cylinders, as well as the assumption of one dimensional flow within a tube. All these approximations can be justified by the impressive results of the model. They are also necessary to keep the computational cost down as simulations of large networks would take prohibitively long. Nonetheless there may be situations where the simplifications result in erronous results, particularly the one dimensional flow approximation is troubling.

In the model any non-wetting bubble occupies the entire width of a tube. This means that the model does not allow for film flow, where the wetting liquid flows along the pore wall while the non-wetting fluid

occupies the bulk of the pore. Film flow is a complicated phenomenon that it is hard to include in a simple network model, however it could significantly influence the results, particularly at low capillary numbers. Film flow would allow wetting fluid to flow passed trapped bubbles of the non-wetting phase. This would, among other things, allow mergers between some trapped bubbles that would be impossible with the current model. Film flow is more important at lower injection rates and the effects are probably negligible for burst dynamics at the injection rates used in this thesis, however some film flow effects were observed by Tallakstad at capillary numbers comparable to the ones used in the simulations [39].

Data analysis related error sources

In all data analysis it has been assumed that the valley size of a burst, χ, is proportional to the geometric burst size, s. This connection has been established experimentally by Furuberg et. al. [17], however this connection was made for slow drainage during an invasion experiment. It has not been established that the result can be generalized to steady state flow with simultaneous injection. This has been assumed in this thesis, and it seems probable that this connection exists during steady state flow as well as the linear pressure increase with injected volume that was used to justify the relation exists during simultaneous injection as well.

The existence of very large valley sizes clearly disconnected from the geometric burst size was mentioned in section 3.4. These should be very infrequent and should therefore not significantly influence the results directly. However, the size and edges of the bins used to create the χ histogram is related to the largest bursts as every burst is counted. This means that even when using logarithmic binning some histograms may contain almost empty bins, skewing the result of regression. This would increase the uncertainty in the final result.

Uncertainty in the critical exponents

The critical exponent is found from linear regression of the last n bins of the reverse cumulative distribution of χ where n is chosen so that only the bursts larger than the cut off are counted. The linear regression is performed on each dataset in turn and the final regression coefficient is

the mean of these coefficients. The uncertainty in the final result is the standard deviation in the regression coefficients that were averaged to produce the final result.

5 Conclusion

We have conducted multiple simulations of multiphase flow through a two dimensional network model of a porous media with varying capillary number and viscosity ratio. From the simulation results the steady state burst inclusive size distribution has been determined to be a power law with critical exponent $\alpha = -2.034 \pm 0.13$. The distribution is independent of the capillary number and the viscosity ratio. We have also attempted to determine the distribution of exclusive bursts during the invasion phase with simultaneous injection of both the wetting fluid and the non-wetting fluid, however the uncertainty in these results is too large for any definite conclusions to be draw. The distribution of exclusive bursts does appear to be a power law, but more data needs to be collected to verify this and to determine the critical exponent. This data can be collected using the existing model, by either simulating significantly larger networks or by simulating multiple smaller networks.

The spatial pressure variation in the lattice was found to be consistent with Darcy's law, except for boundary condition effects. As most real systems are significantly larger than the simulated 50×100 network the boundary effects should be minimized. To do this only nodes far from the boundary should be sampled. There is currently no method for determining how far from the inlet the fluids reach a properly mixed state. Properly determining the mixing length would make future steady state flow investigations easier as a smaller networks could be simulated, significantly reducing the computational time. Based on the relative deviation we would recommend not using data from the last 20 rows of nodes of the lattice in future simulations. This is because the relative deviation from Darcy's law diverges when approaching the outlet and the flow can not be said to be similar to properly mixed steady state flow we aim to study.

The pressure signal autocorrelation in a single point was computed. In all cases it fell linearly with number of lags. This is the how the autocorrelation behaves for a large collection of functions known as autoregressive functions. The autocorrelation in the pressure change was negatively correlated at one lag. This is expected as the pressure fluctuates around a stable value, however no correlation was found for two and three lags. This is interesting as fluctuations around a mean will usually result in a decaying sine wave like function. Sine wave like behaviour was observed

for larger lags, but not for lag equal to 2 and 3. We can offer no satisfactory explanation for this behaviour, but propose that the effect could be attributed to bursts.

The two point correlation function has been approximated. For large distances the two point correlation scales as a power law with critical exponent $\eta = 1/2$. This is consistent with the general form of the two point correlation function for a two dimensional system with scale free fluctuations in a scalar field.

An interesting avenue of investigation would be the spatial and temporal correlation of bursts during steady state flow. Do large burst generally occur at same place in the media? Are large burst in general followed by a series of smaller bursts? To answer these questions a new method of identifying and measuring the bursts would have to be developed. These questions seem particularly interesting as they invite comparisons to earthquakes which have been vigorously studied and are, like bursts, known to be scale free events [9].

It should be emphasized that all the results are obtained from simulations using a relatively simple network model. Closely related models have yielded very impressive results earlier, however the results still need to be experimentally verified.

References

[1] W. A. Adamson. *Physical chemistry of surfaces*. John Wiley and Sons, 1982.

[2] Eyvind Aker. A simulation model for two-phase flow in porous media. Master's thesis, University of Oslo, December 1996.

[3] Eyvind Aker, Knut Jørgen Måløy, Alex Hansen, and G.George Batrouni. A two-dimensional network simulator for two-phase flow in porous media. *Transport in Porous Media*, 32(2):163–186, 1998.

[4] Eyvind Aker, Knut Jørgen Måløy, and Alex Hansen. Simulating temporal evolution of pressure in two-phase flow in porous media. *Phys. Rev. E*, 58:2217–2226, Aug 1998.

[5] Eyvind Aker, Knut Jørgen Måløy, Alex Hansen, and Soumen Basak. Burst dynamics during drainage displacements in porous media: Simulations and experiments. *EPL (Europhysics Letters)*, 51(1):55, 2000.

[6] DG Avraam, GB Kolonis, TC Roumeliotis, GN Constantinides, and AC Payatakes. Steady-state two-phase flow through planar and nonplanar model porous media. *Transport in porous media*, 16(1):75–101, 1994.

[7] DG Avraam and AC Payatakes. Flow regimes and relative permeabilities during steady-state two-phase flow in porous media. *Journal of fluid mechanics*, 293(1):207–236, 1995.

[8] Per Bak. Self-organized criticality. *Physica A: Statistical Mechanics and its Applications*, 163(1):403 – 409, 1990.

[9] Per Bak, Kim Christensen, Leon Danon, and Tim Scanlon. Unified scaling law for earthquakes. *Physical Review Letters*, 88(17):178501, 2002.

[10] Ghassan George Batrouni and Alex Hansen. Fourier acceleration of iterative processes in disordered systems. *Journal of statistical physics*, 52(3-4):747–773, 1988.

[11] M. Bracke, F. Voeght, and P. Joos. The kinetics of wetting: the dynamic contact angle. In P. Bothorel and E.J. Dufourc, editors, *Trends in Colloid and Interface Science III*, volume 79 of *Progress in Colloid & Polymer Science*, pages 142–149. Steinkopff, 1989.

[12] Jing-Den Chen and David Wilkinson. Pore-scale viscous fingering in porous media. *Physical review letters*, 55(18):1892–1895, 1985.

[13] Marek Cieplak and Mark O Robbins. Dynamical transition in quasistatic fluid invasion in porous media. *Physical review letters*, 60(20):2042–2045, 1988.

[14] Arthur K Doolittle. Studies in newtonian flow. i. the dependence of the viscosity of liquids on temperature. *Journal of Applied Physics*, 22(8):1031–1035, 1951.

[15] Marion Erpelding, Santanu Sinha, Ken Tore Tallakstad, Alex Hansen, and Knut Jørgen Måløy. History-independence of steady state in simultaneous two-phase flow through porous media. Submitted to Physical Review E. arXiv:1304.4753, 2013.

[16] Vidar Frette, Kim Christensen, Anders Malthe-Sørenssen, Jens Feder, Torstein Jøssang, and Paul Meakin. Avalanche dynamics in a pile of rice. *Nature*, 379(6560):49–52, 1996.

[17] Liv Furuberg, Knut Jørgen Måløy, and Jens Feder. Intermittent behavior in slow drainage. *Physical Review E*, 53(1):966, 1996.

[18] William B Haines. Studies in the physical properties of soil. v. the hysteresis effect in capillary properties, and the modes of moisture distribution associated therewith. *The Journal of Agricultural Science*, 20(01):97–116, 1930.

[19] Per C Hemmer and Alex Hansen. The distribution of simultaneous fiber failures in fiber bundles. *Journal of applied mechanics*, 59(4):909–914, 1992.

[20] S Irmay. On the theoretical derivation of darcy and forchheimer formulas. *Transactions, American Geophysical Union*, 39:702–707, 1958.

[21] Erwin Kreyszig. *Advanced enigneering mathematics*. John Wiley & Sons, 9 edition, 2008.

[22] P. Lehmann, F. Moebius, F. Hoogland, and D. Or. Fundamentals of air invasion and front displacement processes in porous media. Poster presented at Interpore, 2013-5-23, Prague, Czech Republic, 2013.

[23] R Lenormand, C Zarcone, and A Sarr. Mechanisms of the displacement of one fluid by another in a network of capillary ducts. *J. Fluid Mech*, 135(34):337–353, 1983.

[24] Roland Lenormand, Eric Touboul, and Cesar Zarcone. Numerical models and experiments on immiscible displacements in porous media. *Journal of Fluid Mechanics*, 189(9):165–187, 1988.

[25] Roland Lenormand and Cesar Zarcone. Invasion percolation in an etched network: measurement of a fractal dimension. *Physical review letters*, 54(20):2226–2229, 1985.

[26] Helmut Lütkepohl. Comparison of criteria for estimating the order of a vector autoregressive process. *Journal of time series analysis*, 6(1):35–52, 1985.

[27] Sergei Maslov. Time directed avalanches in invasion models. *Physical review letters*, 74(4):562–565, 1995.

[28] Barry M McCoy. *Advanced Statistical Mechanics*, chapter 10. Oxoford University Press, USA, 2010.

[29] Franziska Moebius and Dani Or. Interfacial jumps and pressure bursts during fluid displacement in interacting irregular capillaries. *Journal of colloid and interface science*, 2012.

[30] Knut Jørgen Måløy, Jens Feder, and Torstein Jøssang. Viscous fingering fractals in porous media. *Physical review letters*, 55(24):2688–2691, 1985.

[31] Knut Jørgen Måløy, Liv Furuberg, Jens Feder, and Torstein Jøssang. Dynamics of slow drainage in porous media. *Physical review letters*, 68(14):2161–2164, 1992.

[32] JS Osoba, JG Richardson, JK Kerver, JA Hafford, and PM Blair. Laboratory measurements of relative permeability. *Journal of Petroleum Technology*, 3(2):47–56, 1951.

[33] Lincoln Paterson. Radial fingering in a hele shaw cell. *Journal of Fluid Mechanics*, 113(1):513–529, 1981.

[34] Lincoln Paterson. Diffusion-limited aggregation and two-fluid displacements in porous media. *Physical review letters*, 52(18):1621–1624, 1984.

[35] JF Poco, JH Satcher Jr, and LW Hrubesh. Synthesis of high porosity, monolithic alumina aerogels. *Journal of non-crystalline solids*, 285(1):57–63, 2001.

[36] JG Richardson, JK Kerver, JA Hafford, and JS Osoba. Laboratory determination of relative permeability. *Journal of Petroleum Technology*, 4(8):187–196, 1952.

[37] A. E. Scheidegger. *The physics of flow through porous media*. University of Toronto Press, third edition edition, 1974.

[38] Jonathan Richard Shewchuk. An introduction to the conjugate gradient method without the agonizing pain, 1994.

[39] Ken Tore Tallakstad. Steady-state, simultaneous two-phase flow in porous media. Master's thesis, University of Oslo, May 2007.

[40] Ken Tore Tallakstad, Grunde Løvoll, Henning Arendt Knudsen, Thomas Ramstad, Eirik Grude Flekkøy, and Knut Jørgen Måløy. Steady-state, simultaneous two-phase flow in porous media: An experimental study. *Physical Review E*, 80(3):036308, 2009.

[41] Aytekin Timur. Effective porosityand permeability of sandstones investigated through nuclear magnetic resonance principles. 1969.

[42] Edward W Washburn. The dynamics of capillary flow. *Physical review*, 17(3):273, 1921.

[43] David Wilkinson and Jorge F Willemsen. Invasion percolation: a new form of percolation theory. *Journal of Physics A: Mathematical and General*, 16(14):3365, 1983.

[44] TA Witten Jr and nard M Sander. Diffusion-limited aggregation, a kinetic critical phenomenon. *Physical Review Letters*, 47(19):1400–1403, 1981.

A Rotated regular lattices

A.1 Rotated lattice

The model presents a simple rotated lattice to represent the porous media. As several operations of interest are significantly more complicated on a rotate lattice than a regular one, a coordinate system rotation is performed.

$$\mathbf{A}\mathbf{x} = \mathbf{x}' \tag{A.1}$$

with vector $\mathbf{x}^T = [x, y]$ and the rotation matrix $\mathbf{A}$ defined by

$$\mathbf{A} = \begin{pmatrix} \cos\theta & \sin\theta \\ -\sin\theta & \cos\theta \end{pmatrix} \tag{A.2}$$

Using the rotation angle of 45° equation A.2 results in

$$\mathbf{A} = \frac{\sqrt{2}}{2}\begin{pmatrix} 1 & 1 \\ -1 & 1 \end{pmatrix} \tag{A.3}$$

Applying this matrix to the original coordinate vector $\mathbf{x}$ and scaling by a constant factor results in

$$\mathbf{x}' = \frac{1}{2}\begin{pmatrix} x+y \\ y-x \end{pmatrix} \tag{A.4}$$

where x and y are the old coordinates.

A.2 Shortest path

The length of the shortest possible path between two points on regular lattice is simply the sum of the difference in each direction. $L = |\Delta x| + |\Delta y|$. Using the coordinate system rotation from section A.1 this results in.

$$L = \Delta x' + \Delta y' \tag{A.5}$$

$$L = \left|\frac{\Delta x + \Delta y}{2}\right| + \left|\frac{\Delta y - \Delta x}{2}\right| \tag{A.6}$$

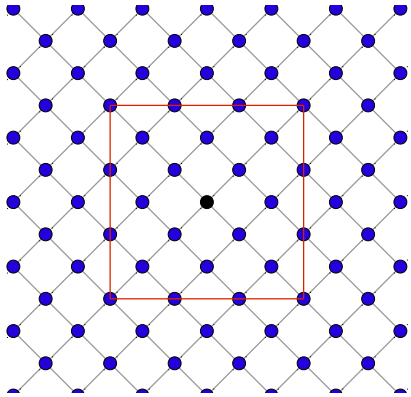

Figure A.1: Equidistant points on a rotated lattice

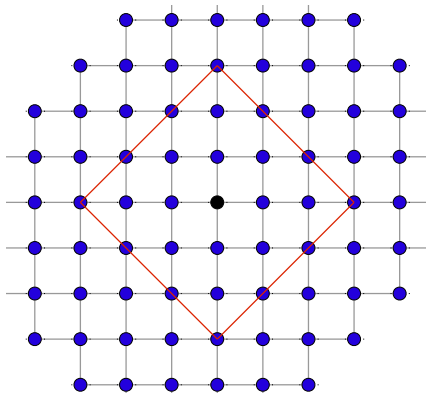

Figure A.2: Equidistant points on a regular lattice

Figure A.1 and A.2 shows a rotated and a regular lattice respectively. In each figure a red square has been overlaid to indicate nodes that are equidistant, in number of edges, from the center node.

A.3 Number of paths

As demonstrated in section A.2 the length between two points on a regular grid depends on the sum of the difference in coordinates. This means that from any point p there are several points p'_i a length L away.

An expression for the number of shortest possible paths between two points p and p' on a regular lattice can be derived by the following argumet. Let $p = (x, y)$ and $p' = (x + m, y + n)$. A path P_0 can be constructed between p and p'. Now assume $m > n$, this can be assumed without loss of generality because if $m < n$ one can switch the x and y coordinate. The shortest path constructed of only steps in the x and y direction must consist of m unit steps in the x direction and n unit steps in the y direction. Furthermore any path constructed in such a way must be equally long. This means that the shortest path problem is equivalent with selecting n from $m + n$ possibilities. That means that the number of possible paths n_P is

$$n_P = \binom{m+n}{n} \tag{A.7}$$

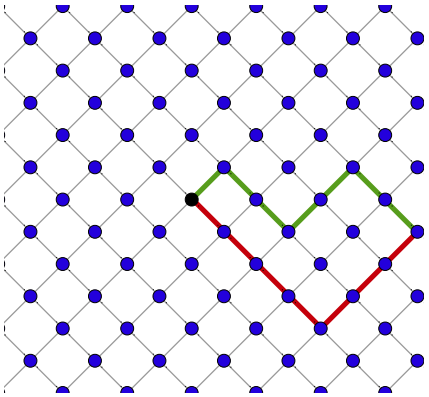

Figure A.3: Two equally long paths on a rotated Lattice

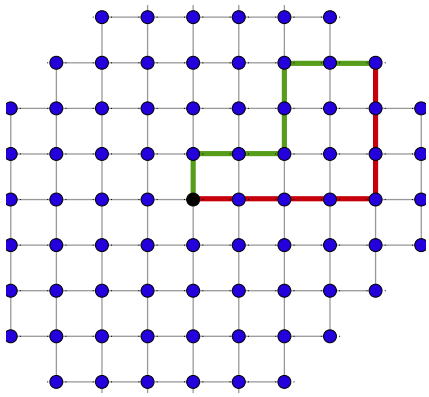

Figure A.4: Two equally long paths on a regular Lattice

Figure A.3 and A.4 display two different equal length paths between two nodes on the rotated grid and the regular grid respectively.

B The Conjugate Gradient Algorithm

This section is based on the discussion found in reference [10] and [38]. The Conjugate Gradient Method is an iterative linear algebra method that solves problems of the form

$$A\mathbf{x} = \mathbf{b} \tag{B.1}$$

where A is a square, symmetric and positive definite matrix. Furthermore the method is very effective if the matrix is sparse.

There are many methods that solve this problem, one of theses methods is the Steepest Descent method which solves the problem iteratively by minimizing the function

$$f(x) = \frac{1}{2}\mathbf{x}^T A\mathbf{x} - \mathbf{x}^T\mathbf{b} \tag{B.2}$$

The vector $\mathbf{x}$ that minimizes equation B.2 is also the solution to equation B.1. The Steepest Descent method minimizes equation B.2 by moving the vector $\mathbf{x}$ along the gradient. This will in many cases lead to very slow convergence. The Conjugate Gradient Algorithm also aims to minimize equation B.2, however it improves on the Steepest Descent alorithm by searching in carefully selected orthogonal directions.

The actual implementation of the algorithm for minimizing equation B.2 is now presented. Start by choosing a set of pressures P_j^0, then compute

$$p_i^0 = r_i^0 = B_i - \sum_j D_{i,j} P_j^0 \tag{B.3}$$

If $p_i^0 = 0$ for all i then the initial guess P^0 is the correct solution. Otherwise compute

$$a^m = \frac{\sum_j r_j^m r_j^m}{\sum_j \sum_k p_j^m D_{j,k} p_k^m} \tag{B.4}$$

$$P_i^{m+1} = P_i^m + a^m p_i^m \tag{B.5}$$

$$r_i^{m+1} = r_i^m - a^m \sum_j D_{i,j} p_j^m \tag{B.6}$$

$$b^m = \frac{\sum_j r_j^{m+1} r_j^{m+1}}{\sum_j r_j^m r_j^m} \tag{B.7}$$

$$p_i^{m+1} = r_i^{m+1} + b^m p_i^m \tag{B.8}$$

As the conjugate gradient method is an iterative process an accuracy criterion must be enforced. The norm of r_i^m is the natural error criterion. Therefore the algorithm has reached desired accuracy when

$$\sum_j r_j^m r_j^m \leq \epsilon^2 \tag{B.9}$$

Where ϵ is the desired accuracy. If the desired accuracy has not been reached repeat equation B.4 to B.8 and check again.

C Specification of boundary conditions of the lattice

In this section the full target vector and permeability matrix will be presented for a small 3×3 system.

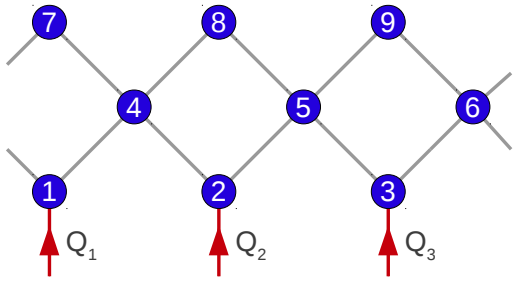

Figure C.1: Small 3×3 grid with periodic boundary conditions in the horizontal direction and a flow imposed on the bottom nodes.

By introducing the value κ the full permeability matrix for this system can be presented. $\kappa_{i,j}$ is defined by

$$\kappa_{i,j} = \frac{k_{i,j}\sigma_{i,j}}{\mu_{i,j}} \tag{C.1}$$

where the subscript i, j indicate the pore between node i and node j. The full permeability matrix and pressure vector for the system in figure C.1 is then

$$\begin{pmatrix} \kappa_{1,6}+\kappa_{1,4} & 0 & 0 & -\kappa_{1,4} & 0 & -\kappa_{1,6} & 0 & 0 & 0 \\ 0 & \kappa_{2,4}+\kappa_{2,5} & 0 & -\kappa_{2,4} & -\kappa_{2,5} & 0 & 0 & 0 & 0 \\ 0 & 0 & \kappa_{3,5}+\kappa_{3,6} & 0 & -\kappa_{3,5} & -\kappa_{3,6} & 0 & 0 & 0 \\ -\kappa_{4,1} & -\kappa_{4,2} & 0 & \kappa_{4,1}+\kappa_{4,2}+\kappa_{4,7}+\kappa_{4,8} & 0 & 0 & -\kappa_{4,7} & \kappa_{4,8} & 0 \\ 0 & -\kappa_{5,2} & -\kappa_{5,3} & 0 & \kappa_{5,2}+\kappa_{5,3}+\kappa_{5,8}+\kappa_{5,9} & 0 & 0 & -\kappa_{5,8} & -\kappa_{5,9} \\ -\kappa_{6,1} & 0 & -\kappa_{6,3} & 0 & 0 & \kappa_{6,3}+\kappa_{6,1}+\kappa_{6,9}+\kappa_{6,7} & -\kappa_{6,7} & 0 & -\kappa_{6,9} \\ 0 & 0 & 0 & -\kappa_{7,4} & 0 & -\kappa_{7,6} & \kappa_{7,6}+\kappa_{7,4} & 0 & 0 \\ 0 & 0 & 0 & -\kappa_{8,4} & -\kappa_{8,5} & 0 & 0 & \kappa_{8,4}+\kappa_{8,5} & 0 \\ 0 & 0 & 0 & 0 & -\kappa_{9,5} & -\kappa_{9,6} & 0 & 0 & \kappa_{9,5}+\kappa_{9,6} \end{pmatrix} \begin{pmatrix} p_1 \\ p_2 \\ p_3 \\ p_4 \\ p_5 \\ p_6 \\ p_7 \\ p_8 \\ p_9 \end{pmatrix} = \begin{pmatrix} p^c_{1,6}+p^c_{1,4}+Q_1 \\ p^c_{2,4}+p^c_{2,5}+Q_2 \\ p^c_{3,5}+p^c_{3,6}+Q_3 \\ p^c_{4,1}+p^c_{4,2}+p^c_{4,7}+p^c_{4,8} \\ p^c_{5,2}+p^c_{5,3}+p^c_{5,8}+p^c_{5,9} \\ p^c_{6,1}+p^c_{6,3}+p^c_{6,7}+p^c_{6,9} \\ p^c_{7,4}+p^c_{7,6} \\ p^c_{8,4}+p^c_{8,5} \\ p^c_{9,5}+p^c_{9,6} \end{pmatrix}$$

with the target vector contains the capillary pressure in each pore associated with the relevant node and the imposed constant flow on node $1-3$.

D Logarithmic binning

Given a random variable X with some probability density function (PDF) $f_X(x)$ the probability that a sample of X lies on the interval $x < X < x + dx$ is defined as

$$\Pr(x < X < x + dx) = f_X(x)dx \tag{D.1}$$

If the probability density function is unknown it can be found by sampling the random variable multiple times and constructing a histogram of the results. The histogram consists of a set of bins, where each sample of the random variable is added to the bin corresponding to the value of the sample. It is evident that the number of samples in each bin, n_i, is proportional to the probability density function of the random variable and the width of the bin, w_i.

$$n_i \propto w_i f_X(x) \tag{D.2}$$

If the PDF of the random variable is a exponential function, $f_X(x) \propto x^{-\alpha}$, the exponent α is found by regressing $\log(n)$ versus $\log(x)$

$$\log(n_i) \propto \log(w_i f_X(x)) \tag{D.3a}$$
$$\log(n_i) \propto \log(w_i x^{\alpha}) \tag{D.3b}$$

If the bin width is some constant, $w_i = b$, then equation D.3b results in

$$\log(n_i) \propto \log(b) + \alpha \log(x) \tag{D.4}$$

This regression would result in the correct value α. However as the PDF is an exponential function it may be several orders of magnitude larger for the smallest sample than the largest sample. This difference will directly carry over to the histogram with some bins containing several

orders of magnitude more samples than others, and it is probable that some bins contain 0 samples. This reduces the accuracy of the regression and to avoid it logarithmic binning is used.

Logarithmic binning means that the logarithm of the lower edge of bin i and the logarithm of the lower edge of bin $i+1$ is separated by a distance b

$$\log(x_{i+1}) = log(x_i) + b \tag{D.5}$$

Exponentiating both sides results in

$$x_{i+1} = x_i e^b \tag{D.6}$$

Giving a bin width w_i

$$w_i = x_i \left(e^b - 1\right) \tag{D.7}$$

Inserting equation D.7 into equation D.3b and assuming $f_X(x) \propto x^\alpha$ results in

$$\log(n_i) \propto \log(x_i x_i^\alpha) \tag{D.8a}$$
$$\log(n_i) \propto (\alpha + 1)\log(x_i) \tag{D.8b}$$

This means that the exponent differs by one between logarithmic binning and constant binning.

E Geometric invasion modelling

E.1 Invasion percolation

Invasion percolation is a geometrical process that accurately models capillary fingering. The algorithm is given by:

1. Each site on a $L_x \times L_y$ lattice is assigned a random threshold on the unit interval.

2. Each site on the bottom row is set to one, all other sites set to zero.

3. The zero-value-site adjacent to a one-value-site with the lowest threshold is set to one.

4. (Optional) If a region of zero-value-sites is completely surrounded by one-value-sites then these sites are assigned threshold 1, making invasion impossible.

5. Repeat step 3. and 4. until a site at the top row has been set to one.

E.2 Diffusion limited aggregation

Diffusion limited aggregation is a geometric process that accurately models viscous fingering. The algorithm is given by:

1. A single site on the bottom row on a $L_x \times L_y$ lattice is set to one, all other sites are set to zero.

2. A random-walker is introduced at the top row. When the walker reaches a site adjacent to a one-value-site it stops and this site is set to one. The walker can only move to adjacent sites of its current position , it can never leave the lattice.

3. Repeat step 2. until a site at the top row is set to one.

E.3 Anti diffusion limited aggregation

Anti diffusion limited aggregation is a geometric process that accurately models stable displacement. The algorithm is given by:

1. Set all sites on a $L_x \times L_y$ lattice to one.

2. Release a random walker at the bottom row. When the walker reaches a one-value-site it stops and the site is set to zero. The walker can only move to adjacent sites of its current position , it can never leave the lattice.

3. Repeat step 3. until a site at the top row is set to zero.